Search for Higgs boson production in oppositely charged dilepton and missing energy final states in 9.7 fb-1 of ppbar collisions at sqrts = 1.96 TeV

V.M. Abazov, U. Bassler, G. Bernardi, M. Besançon, D. Brown, J. Brown, E. Chapon, F. Couderc, F. Deliot, Y. Enari, et al.

Search for Higgs boson production in oppositely charged dilepton and missing energy final states in 9.7 fb^{-1} of $p\bar{p}$ collisions at $\sqrt{s} = 1.96$ TeV

V.M. Abazov,[32] B. Abbott,[68] B.S. Acharya,[26] M. Adams,[46] T. Adams,[44] G.D. Alexeev,[32] G. Alkhazov,[36] A. Alton[a],[57] A. Askew,[44] S. Atkins,[55] K. Augsten,[7] C. Avila,[5] F. Badaud,[10] L. Bagby,[45] B. Baldin,[45] D.V. Bandurin,[44] S. Banerjee,[26] E. Barberis,[56] P. Baringer,[53] J.F. Bartlett,[45] U. Bassler,[15] V. Bazterra,[46] A. Bean,[53] M. Begalli,[2] L. Bellantoni,[45] S.B. Beri,[24] G. Bernardi,[14] R. Bernhard,[19] I. Bertram,[39] M. Besançon,[15] R. Beuselinck,[40] P.C. Bhat,[45] S. Bhatia,[59] V. Bhatnagar,[24] G. Blazey,[47] S. Blessing,[44] K. Bloom,[60] A. Boehnlein,[45] D. Boline,[65] E.E. Boos,[34] G. Borissov,[39] A. Brandt,[71] O. Brandt,[20] R. Brock,[58] A. Bross,[45] D. Brown,[14] J. Brown,[14] X.B. Bu,[45] M. Buehler,[45] V. Buescher,[21] V. Bunichev,[34] S. Burdin[b],[39] C.P. Buszello,[38] E. Camacho-Pérez,[29] B.C.K. Casey,[45] H. Castilla-Valdez,[29] S. Caughron,[58] S. Chakrabarti,[65] D. Chakraborty,[47] K.M. Chan,[51] A. Chandra,[73] E. Chapon,[15] G. Chen,[53] S.W. Cho,[28] S. Choi,[28] B. Choudhary,[25] S. Cihangir,[45] D. Claes,[60] J. Clutter,[53] M. Cooke,[45] W.E. Cooper,[45] M. Corcoran,[73] F. Couderc,[15] M.-C. Cousinou,[12] D. Cutts,[70] A. Das,[42] G. Davies,[40] S.J. de Jong,[30, 31] E. De La Cruz-Burelo,[29] F. Déliot,[15] R. Demina,[64] D. Denisov,[45] S.P. Denisov,[35] S. Desai,[45] C. Deterre[d],[20] K. DeVaughan,[60] H.T. Diehl,[45] M. Diesburg,[45] P.F. Ding,[41] A. Dominguez,[60] A. Dubey,[25] L.V. Dudko,[34] D. Duggan,[61] A. Duperrin,[12] S. Dutt,[24] A. Dyshkant,[47] M. Eads,[47] D. Edmunds,[58] J. Ellison,[43] V.D. Elvira,[45] Y. Enari,[14] H. Evans,[49] V.N. Evdokimov,[35] G. Facini,[56] A. Fauré,[15] L. Feng,[47] T. Ferbel,[64] F. Fiedler,[21] F. Filthaut,[30, 31] W. Fisher,[58] H.E. Fisk,[45] M. Fortner,[47] H. Fox,[39] S. Fuess,[45] A. Garcia-Bellido,[64] J.A. García-González,[29] G.A. García-Guerra[c],[29] V. Gavrilov,[33] W. Geng,[12, 58] C.E. Gerber,[46] Y. Gershtein,[61] G. Ginther,[45, 64] G. Golovanov,[32] P.D. Grannis,[65] S. Greder,[16] H. Greenlee,[45] G. Grenier,[17] Ph. Gris,[10] J.-F. Grivaz,[13] A. Grohsjean[d],[15] S. Grünendahl,[45] M.W. Grünewald,[27] T. Guillemin,[13] G. Gutierrez,[45] P. Gutierrez,[68] J. Haley,[56] L. Han,[4] K. Harder,[41] A. Harel,[64] J.M. Hauptman,[52] J. Hays,[40] T. Head,[41] T. Hebbeker,[18] D. Hedin,[47] H. Hegab,[69] A.P. Heinson,[43] U. Heintz,[70] C. Hensel,[20] I. Heredia-De La Cruz,[29] K. Herner,[57] G. Hesketh[f],[41] M.D. Hildreth,[51] R. Hirosky,[74] T. Hoang,[44] J.D. Hobbs,[65] B. Hoeneisen,[9] J. Hogan,[73] M. Hohlfeld,[21] I. Howley,[71] Z. Hubacek,[7, 15] V. Hynek,[7] I. Iashvili,[63] Y. Ilchenko,[72] R. Illingworth,[45] A.S. Ito,[45] S. Jabeen,[70] M. Jaffré,[13] A. Jayasinghe,[68] M.S. Jeong,[28] R. Jesik,[40] P. Jiang,[4] K. Johns,[42] E. Johnson,[58] M. Johnson,[45] A. Jonckheere,[45] P. Jonsson,[40] J. Joshi,[43] A.W. Jung,[45] A. Juste,[37] E. Kajfasz,[12] D. Karmanov,[34] P.A. Kasper,[45] I. Katsanos,[60] R. Kehoe,[72] S. Kermiche,[12] N. Khalatyan,[45] A. Khanov,[69] A. Kharchilava,[63] Y.N. Kharzheev,[32] I. Kiselevich,[33] J.M. Kohli,[24] A.V. Kozelov,[35] J. Kraus,[59] A. Kumar,[63] A. Kupco,[8] T. Kurča,[17] V.A. Kuzmin,[34] S. Lammers,[49] G. Landsberg,[70] P. Lebrun,[17] H.S. Lee,[28] S.W. Lee,[52] W.M. Lee,[44] X. Lei,[42] J. Lellouch,[14] D. Li,[14] H. Li,[74] L. Li,[43] Q.Z. Li,[45] J.K. Lim,[28] D. Lincoln,[45] J. Linnemann,[58] V.V. Lipaev,[35] R. Lipton,[45] H. Liu,[72] Y. Liu,[4] A. Lobodenko,[36] M. Lokajicek,[8] R. Lopes de Sa,[65] R. Luna-Garcia[g],[29] A.L. Lyon,[45] A.K.A. Maciel,[1] R. Magaña-Villalba,[29] S. Malik,[60] V.L. Malyshev,[32] Y. Maravin,[54] J. Martínez-Ortega,[29] R. McCarthy,[65] C.L. McGivern,[41] M.M. Meijer,[30, 31] A. Melnitchouk,[45] D. Menezes,[47] P.G. Mercadante,[3] M. Merkin,[34] A. Meyer,[18] J. Meyer,[20] F. Miconi,[16] N.K. Mondal,[26] M. Mulhearn,[74] E. Nagy,[12] M. Naimuddin,[25] M. Narain,[70] R. Nayyar,[42] H.A. Neal,[57] J.P. Negret,[5] P. Neustroev,[36] H.T. Nguyen,[74] T. Nunnemann,[22] J. Orduna,[73] N. Osman,[12] J. Osta,[51] M. Padilla,[43] A. Pal,[71] N. Parashar,[50] V. Parihar,[70] S.K. Park,[28] R. Partridge[e],[70] N. Parua,[49] A. Patwa,[66] B. Penning,[45] M. Perfilov,[34] Y. Peters,[20] K. Petridis,[41] G. Petrillo,[64] P. Pétroff,[13] M.-A. Pleier,[66] P.L.M. Podesta-Lerma[h],[29] V.M. Podstavkov,[45] A.V. Popov,[35] M. Prewitt,[73] D. Price,[49] N. Prokopenko,[35] J. Qian,[57] A. Quadt,[20] B. Quinn,[59] M.S. Rangel,[1] K. Ranjan,[25] P.N. Ratoff,[39] I. Razumov,[35] P. Renkel,[72] I. Ripp-Baudot,[16] F. Rizatdinova,[69] M. Rominsky,[45] A. Ross,[39] C. Royon,[15] P. Rubinov,[45] R. Ruchti,[51] G. Sajot,[11] P. Salcido,[47] A. Sánchez-Hernández,[29] M.P. Sanders,[22] A.S. Santos[i],[1] G. Savage,[45] L. Sawyer,[55] T. Scanlon,[40] R.D. Schamberger,[65] Y. Scheglov,[36] H. Schellman,[48] C. Schwanenberger,[41] R. Schwienhorst,[58] J. Sekaric,[53] H. Severini,[68] E. Shabalina,[20] V. Shary,[15] S. Shaw,[58] A.A. Shchukin,[35] R.K. Shivpuri,[25] V. Simak,[7] P. Skubic,[68] P. Slattery,[64] D. Smirnov,[51] K.J. Smith,[63] G.R. Snow,[60] J. Snow,[67] S. Snyder,[66] S. Söldner-Rembold,[41] L. Sonnenschein,[18] K. Soustruznik,[6] J. Stark,[11] D.A. Stoyanova,[35] M. Strauss,[68] L. Suter,[41] P. Svoisky,[68] M. Titov,[15] V.V. Tokmenin,[32] Y.-T. Tsai,[64] D. Tsybychev,[65] B. Tuchming,[15] C. Tully,[62] L. Uvarov,[36] S. Uvarov,[36] S. Uzunyan,[47] R. Van Kooten,[49] W.M. van Leeuwen,[30] N. Varelas,[46] E.W. Varnes,[42] I.A. Vasilyev,[35] P. Verdier,[17]

A.Y. Verkheev,[32] L.S. Vertogradov,[32] M. Verzocchi,[45] M. Vesterinen,[41] D. Vilanova,[15] P. Vokac,[7] H.D. Wahl,[44]
M.H.L.S. Wang,[45] J. Warchol,[51] G. Watts,[75] M. Wayne,[51] J. Weichert,[21] L. Welty-Rieger,[48] A. White,[71]
D. Wicke,[23] M.R.J. Williams,[39] G.W. Wilson,[53] M. Wobisch,[55] D.R. Wood,[56] T.R. Wyatt,[41] Y. Xie,[45]
R. Yamada,[45] S. Yang,[4] T. Yasuda,[45] Y.A. Yatsunenko,[32] W. Ye,[65] Z. Ye,[45] H. Yin,[45] K. Yip,[66] S.W. Youn,[45]
J.M. Yu,[57] J. Zennamo,[63] T.G. Zhao,[41] B. Zhou,[57] J. Zhu,[57] M. Zielinski,[64] D. Zieminska,[49] and L. Zivkovic[14]

(The D0 Collaboration[*])

[1]LAFEX, Centro Brasileiro de Pesquisas Físicas, Rio de Janeiro, Brazil
[2]Universidade do Estado do Rio de Janeiro, Rio de Janeiro, Brazil
[3]Universidade Federal do ABC, Santo André, Brazil
[4]University of Science and Technology of China, Hefei, People's Republic of China
[5]Universidad de los Andes, Bogotá, Colombia
[6]Charles University, Faculty of Mathematics and Physics,
Center for Particle Physics, Prague, Czech Republic
[7]Czech Technical University in Prague, Prague, Czech Republic
[8]Center for Particle Physics, Institute of Physics,
Academy of Sciences of the Czech Republic, Prague, Czech Republic
[9]Universidad San Francisco de Quito, Quito, Ecuador
[10]LPC, Université Blaise Pascal, CNRS/IN2P3, Clermont, France
[11]LPSC, Université Joseph Fourier Grenoble 1, CNRS/IN2P3,
Institut National Polytechnique de Grenoble, Grenoble, France
[12]CPPM, Aix-Marseille Université, CNRS/IN2P3, Marseille, France
[13]LAL, Université Paris-Sud, CNRS/IN2P3, Orsay, France
[14]LPNHE, Universités Paris VI and VII, CNRS/IN2P3, Paris, France
[15]CEA, Irfu, SPP, Saclay, France
[16]IPHC, Université de Strasbourg, CNRS/IN2P3, Strasbourg, France
[17]IPNL, Université Lyon 1, CNRS/IN2P3, Villeurbanne, France and Université de Lyon, Lyon, France
[18]III. Physikalisches Institut A, RWTH Aachen University, Aachen, Germany
[19]Physikalisches Institut, Universität Freiburg, Freiburg, Germany
[20]II. Physikalisches Institut, Georg-August-Universität Göttingen, Göttingen, Germany
[21]Institut für Physik, Universität Mainz, Mainz, Germany
[22]Ludwig-Maximilians-Universität München, München, Germany
[23]Fachbereich Physik, Bergische Universität Wuppertal, Wuppertal, Germany
[24]Panjab University, Chandigarh, India
[25]Delhi University, Delhi, India
[26]Tata Institute of Fundamental Research, Mumbai, India
[27]University College Dublin, Dublin, Ireland
[28]Korea Detector Laboratory, Korea University, Seoul, Korea
[29]CINVESTAV, Mexico City, Mexico
[30]Nikhef, Science Park, Amsterdam, the Netherlands
[31]Radboud University Nijmegen, Nijmegen, the Netherlands
[32]Joint Institute for Nuclear Research, Dubna, Russia
[33]Institute for Theoretical and Experimental Physics, Moscow, Russia
[34]Moscow State University, Moscow, Russia
[35]Institute for High Energy Physics, Protvino, Russia
[36]Petersburg Nuclear Physics Institute, St. Petersburg, Russia
[37]Institució Catalana de Recerca i Estudis Avançats (ICREA) and Institut de Física d'Altes Energies (IFAE), Barcelona, Spain
[38]Uppsala University, Uppsala, Sweden
[39]Lancaster University, Lancaster LA1 4YB, United Kingdom
[40]Imperial College London, London SW7 2AZ, United Kingdom
[41]The University of Manchester, Manchester M13 9PL, United Kingdom
[42]University of Arizona, Tucson, Arizona 85721, USA
[43]University of California Riverside, Riverside, California 92521, USA
[44]Florida State University, Tallahassee, Florida 32306, USA
[45]Fermi National Accelerator Laboratory, Batavia, Illinois 60510, USA
[46]University of Illinois at Chicago, Chicago, Illinois 60607, USA
[47]Northern Illinois University, DeKalb, Illinois 60115, USA
[48]Northwestern University, Evanston, Illinois 60208, USA
[49]Indiana University, Bloomington, Indiana 47405, USA
[50]Purdue University Calumet, Hammond, Indiana 46323, USA
[51]University of Notre Dame, Notre Dame, Indiana 46556, USA
[52]Iowa State University, Ames, Iowa 50011, USA
[53]University of Kansas, Lawrence, Kansas 66045, USA

^{54}*Kansas State University, Manhattan, Kansas 66506, USA*
^{55}*Louisiana Tech University, Ruston, Louisiana 71272, USA*
^{56}*Northeastern University, Boston, Massachusetts 02115, USA*
^{57}*University of Michigan, Ann Arbor, Michigan 48109, USA*
^{58}*Michigan State University, East Lansing, Michigan 48824, USA*
^{59}*University of Mississippi, University, Mississippi 38677, USA*
^{60}*University of Nebraska, Lincoln, Nebraska 68588, USA*
^{61}*Rutgers University, Piscataway, New Jersey 08855, USA*
^{62}*Princeton University, Princeton, New Jersey 08544, USA*
^{63}*State University of New York, Buffalo, New York 14260, USA*
^{64}*University of Rochester, Rochester, New York 14627, USA*
^{65}*State University of New York, Stony Brook, New York 11794, USA*
^{66}*Brookhaven National Laboratory, Upton, New York 11973, USA*
^{67}*Langston University, Langston, Oklahoma 73050, USA*
^{68}*University of Oklahoma, Norman, Oklahoma 73019, USA*
^{69}*Oklahoma State University, Stillwater, Oklahoma 74078, USA*
^{70}*Brown University, Providence, Rhode Island 02912, USA*
^{71}*University of Texas, Arlington, Texas 76019, USA*
^{72}*Southern Methodist University, Dallas, Texas 75275, USA*
^{73}*Rice University, Houston, Texas 77005, USA*
^{74}*University of Virginia, Charlottesville, Virginia 22904, USA*
^{75}*University of Washington, Seattle, Washington 98195, USA*
(Dated: January 7, 2013)

We present a search for Higgs boson in final states with two oppositely charged leptons and large missing transverse energy as expected in $H \to WW \to \ell\nu\ell'\nu'$ decays. The events are selected from the full Run II data sample of 9.7 fb^{-1} of $p\bar{p}$ collisions collected with the D0 detector at the Fermilab Tevatron Collider at $\sqrt{s} = 1.96$ TeV. To validate our search methodology, we measure the non-resonant WW production cross section and find $\sigma_{WW} = 11.6 \pm 0.7$ pb, in agreement with the standard model prediction. In the Higgs boson search, no significant excess above the background expectation is observed. Upper limits at the 95% confidence level on the Higgs boson production cross section are therefore derived. Within the standard model, the Higgs boson mass range $159 < M_H < 176$ GeV is excluded while the expected exclusion sensitivity is $156 < M_H < 172$ GeV. For a mass hypothesis of $M_H = 125$ GeV, we exclude Higgs boson production cross sections 4.1 times larger than the standard model expectation, which is compatible with the presence of a Higgs boson at this mass. Within a theoretical framework with a fourth generation of fermions, the mass range $125 < M_H < 218$ GeV is excluded. The search results are also interpreted in the context of fermiophobic Higgs boson couplings, which yields an exclusion of fermiophobic Higgs boson production cross sections 3.1 times larger than the expectation for $M_H = 125$ GeV.

PACS numbers: 14.80.Bn, 13.85.Qk, 13.85.Rm, 14.65.Jk, 14.80.Ec, 14.70.Fm

INTRODUCTION

Spontaneous breaking of the $SU(2) \times U(1)$ electroweak symmetry explains why the W and Z weak vector bosons are massive particles. However the details of the symmetry breaking mechanism are yet to be fully explored. In the standard model (SM), it results from the existence of a single elementary scalar field doublet that acquires a non-zero vacuum expectation value. After accounting for the mass of the weak vector bosons, one

degree of freedom remains, manifesting itself as a single scalar particle, the Higgs boson. Its mass, M_H, is a free parameter of the model. A lower limit of 114.4 GeV was set on M_H by the CERN LEP experiments [1]. This experimental constraint was extended by the combined results from the CDF and D0 experiments that excluded the Higgs boson mass range from 156 GeV to 177 GeV [2, 3]. Upper (lower) limits of 131 (122) GeV [4] and 128 (121.5) GeV [5] have then been established by the ATLAS and CMS Collaborations, respectively. These exclusion limits and those reported hereafter are all defined at the 95% C.L. In both Ref. [4] and Ref. [5], excesses above background expectations at the five standard deviation (s.d.) level have been reported, consistent with the observation of a Higgs boson of $M_H \approx 125$ GeV. The CDF and D0 Collaborations have reported excesses above background expectations in the $H \to b\bar{b}$ search channels [6, 7]. Their combination yields an excess at the three s.d. level, consistent with the production of a

*with visitors from ^{a}Augustana College, Sioux Falls, SD, USA, ^{b}The University of Liverpool, Liverpool, UK, ^{c}UPIITA-IPN, Mexico City, Mexico, ^{d}DESY, Hamburg, Germany, ^{e}SLAC, Menlo Park, CA, USA, ^{f}University College London, London, UK, ^{g}Centro de Investigacion en Computacion - IPN, Mexico City, Mexico, ^{h}ECFM, Universidad Autonoma de Sinaloa, Culiacán, Mexico and ^{i}Universidade Estadual Paulista, São Paulo, Brazil.

Higgs boson of mass $M_H \approx 125$ GeV [8].

In this Letter, we present a search for the SM Higgs boson in final states containing two oppositely charged leptons ($\ell\ell' = e\mu$, ee, or $\mu\mu$, where small contributions from leptonic τ decays are also included) and missing transverse energy ($\not{E}_T$). The search relies on the full Run II data set of 9.7 fb^{-1} of $p\bar{p}$ collisions collected with the D0 detector at the Fermilab Tevatron Collider at $\sqrt{s} = 1.96$ TeV. This analysis supersedes our previously published results in the same final states, obtained after analyzing 5.4 fb^{-1} [9] and 8.6 fb^{-1} [10] of integrated luminosity. A similar search has been conducted by the CDF Collaboration using 4.8 fb^{-1} of integrated luminosity [11]. The results from Refs. [9, 11] have been combined in Ref. [2]. More recently, searches in dilepton plus missing transverse energy final states have been conducted by the ATLAS [12] and CMS [13] Collaborations using 4.7 fb^{-1} and 4.6 fb^{-1} of integrated luminosity, respectively.

The main Higgs boson production and decay channel resulting in opposite charge dilepton plus $\not{E}_T$ final states at the Tevatron is the gluon fusion production, $gg \rightarrow H$, with subsequent decay $H \rightarrow W^+W^- \rightarrow \ell^+\nu\ell'^-\bar{\nu}'$, where one of the W bosons is virtual for $M_H < 160$ GeV. This final state receives additional contributions from Higgs boson production via vector boson fusion (VBF), $q\bar{q}' \rightarrow q\bar{q}'VV \rightarrow q\bar{q}'H$, and from production in association with a vector boson, $q\bar{q}' \rightarrow VH$ ($V = W, Z$). The primary source of background is due to diboson production, in particular the non-resonant $p\bar{p} \rightarrow WW$ process. Other background sources are the Drell-Yan (DY) process, $p\bar{p} \rightarrow Z/\gamma^* \rightarrow \ell\ell$, with a mismeasured $\not{E}_T$, the leptonic decays of top-quark pairs ($t\bar{t}$), W+jets/γ and multijet events in which jets (photons) are misidentified as leptons (electrons).

The initial selection of Higgs boson candidate events is based on the reconstruction of two high transverse momentum (p_T) leptons. This selection is followed by additional requirements, involving $\not{E}_T$, and the usage of multivariate techniques based on boosted decision trees (BDT) [14], to suppress the large DY background. To increase the sensitivity, the events are separately analyzed according to the lepton flavors (ee, $e\mu$, and $\mu\mu$) and jet multiplicity, and they are also categorized into WW-enriched and WW-depleted sub-samples. Additional BDTs are trained to separate the signal from the remaining background events. To demonstrate the validity of the techniques used in this search, we use similar BDTs to measure the cross section for the SM non-resonant WW production cross section. For the Higgs boson searches, the outputs of the BDTs are the final discriminants used for the statistical interpretation of the data, within the SM framework, but also in the contexts of a fourth generation of fermions and a fermiophobic Higgs boson. These models are described in more detail in later sections.

DETECTOR AND OBJECT RECONSTRUCTION

The D0 detector used for Run II (2002 – 2011) is described in detail in Ref. [15]. The innermost part of the detector is composed of a central tracking system with a silicon microstrip tracker (SMT) and a central fiber tracker embedded within a 2 T solenoidal magnet. The tracking system is surrounded by a central preshower detector and a liquid-argon/uranium calorimeter with electromagnetic, fine, and coarse hadronic sections. The central calorimeter (CC) covers pseudorapidity [16] $|\eta| \lesssim 1.1$. Two end calorimeters (EC) extend the coverage to $1.4 \lesssim |\eta| \lesssim 4.2$. The pseudorapidity gap between the ECs and CC is covered by scintillating tiles. A muon spectrometer, with pseudorapidity coverage of $|\eta| \lesssim 2$, resides outside the calorimetry and is comprised of drift tubes, scintillation counters, and toroidal magnets. Trigger decisions are based on information from the tracking detectors, calorimeters, and muon spectrometer.

Electrons are reconstructed as isolated clusters in the electromagnetic calorimeter, and required to spatially match a track in the central tracking system. They have to pass a BDT (ee channel) or likelihood ($e\mu$ channel) criterion (collectively called electron quality later in the text) that accounts for calorimeter shower shape observables, a spatial track match probability estimate, and the ratio of the electron cluster energy to track momentum (E/p). Electrons are required to be in the acceptance of the calorimeter ($|\eta| < 1.1$ or $1.5 < |\eta| < 2.5$). In the dielectron channel, events with one electron in the EC are treated separately from events with both electrons in the CC. Events where both electrons are in the EC are not considered due to a large background and a small signal contribution.

Muons are identified by the presence of at least one track segment reconstructed in the acceptance ($|\eta| < 2.0$) of the muon spectrometer, that is spatially consistent with a track in the central tracking detector. The momentum and charge are measured by the curvature in the central tracking system. To select isolated muons, criteria based on the momenta of central tracks emitted in the approximately same direction as the muon and criteria based on the energy deposited around the muon trajectory in the calorimeter are employed. The number of hits in the wire chambers and in the scintillators are combined to define a muon quality variable used in the final stage of the analysis.

Jets are reconstructed from energy deposits in the calorimeter using an iterative midpoint cone algorithm [17] with a cone radius $\mathcal{R} = 0.5$ [18]. The jet energies are calibrated using transverse momentum balance in γ+jet events [19]. Jets are considered in this analysis only if they have $p_T > 20$ GeV and $|\eta| < 2.4$. Each jet is also required to be matched to at least two tracks associated to the $p\bar{p}$ interaction vertex.

The $\not{E}_T$ and its direction are obtained from the vector sum of the transverse components of energy deposits in the calorimeter, corrected for the differences in detector response of the reconstructed muons, electrons, and jets.

DATA AND SIMULATED SAMPLES

Signal and SM background processes except multijet are simulated with PYTHIA [20] or ALPGEN [21] generators, with PYTHIA providing showering and hadronization in the latter case, using the CTEQ6L1 [22] parton distribution functions (PDFs), followed by a detailed GEANT3-based [23] simulation of the D0 detector. In order to model the effects of multiple $p\bar{p}$ interactions, the Monte-Carlo (MC) samples are overlaid with events from random $p\bar{p}$ collisions with the same luminosity distribution as data. Then, these events are reconstructed with the same software as used for the data. Jet energy calibration and calorimeter response to unclustered objects are adjusted in simulated events to match those measured in data. Corrections for residual differences between data and simulation are applied to electrons, muons, and jets for both identification efficiencies and energy resolutions.

Higgs boson signal samples are simulated using PYTHIA for $100 \leq M_H \leq 200$ GeV in increments of 5 GeV, and for $200 \leq M_H \leq 300$ GeV in increments of 10 GeV. For $gg \rightarrow H$ production, the cross section is calculated at next-to-next-to-leading order with resummed next-to-next-to-leading logarithm (NNLO+NNLL) [24], for VBF at NNLO [25], and for VH at NNLO [26]. All signal cross sections are computed using the MSTW 2008 NNLO PDF set [27]. The distribution of the Higgs boson p_T for $gg \rightarrow H$ process is weighted to match the calculation of the HQT generator, which has NNLO and NNLL accuracy [28]. The Higgs boson branching ratio predictions are taken from HDECAY [29].

The W+jets and Z+jets backgrounds are modeled using ALPGEN. The W+jets and Z+jets processes are normalized using the NNLO cross section calculations of Ref. [30]. The p_T distribution of Z bosons is weighted to match the distribution observed in data [31], taking into account its dependence on the number of reconstructed jets. The p_T distribution of W bosons is weighted to match the measured Z boson p_T spectrum, corrected for the differences between the W and Z p_T spectra predicted in NNLO QCD [32]. In the ee and $e\mu$ channels, the W+jets simulation includes contributions from events where a misidentified electron originates from a jet or a photon. The size of each of these contributions is corrected such that the distribution of the number of hits in the innermost silicon layer, associated to the electron track, matches that observed in a W+jets enriched control sample.

The $t\bar{t}$ process is modeled using ALPGEN with showering and hadronization provided by PYTHIA, and normal-ized to the approximate NNLO cross section [33].

Diboson production processes (WW, WZ, and ZZ) are simulated using PYTHIA, normalized to NLO cross sections [34]. An additional correction, determined using the POWHEG generator [35], accounts for $Z/\gamma^\star$ interference in WZ production. For the irreducible background arising from WW production, the p_T of the diboson system is modeled using the MC@NLO simulation [36], and the distribution of the opening angle of the two leptons is corrected for the contribution of the non-resonant $gg \rightarrow WW$ process [37].

The background due to multijet production, where jets are misidentified as leptons, is determined from data by inverting some of the lepton selection criteria. All other event selection criteria are applied in order to model the kinematic distributions of the multijet background in the signal region. In the $\mu\mu$ channel, the opposite-charge requirement for muons is reversed, and a correction for the presence of non-multijet events in the like-sign sample, estimated from simulation, is applied. For the ee and $e\mu$ channels, the electron quality requirement is reversed, and the normalization is determined from control samples in which the leptons have the same charge.

EVENT PRESELECTION

A first selection is applied on the data by requiring two high-p_T leptons, that have opposite charge and that originate from the same location, within 2 cm, along the beamline. In the ee and $\mu\mu$ channels, the highest-p_T and next highest p_T leptons are required to satisfy $p_T^{\ell 1} > 15$ GeV and $p_T^{\ell 2} > 10$ GeV, whereas in the $e\mu$ channel, $p_T^e > 15$ GeV and $p_T^\mu > 10$ GeV are required. Additionally, in the ee and $\mu\mu$ final states, the dilepton invariant mass $M_{\ell\ell}$ is required to be greater than 15 GeV. A veto against additional leptons is applied to prevent overlap with dedicated Higgs searches in trilepton final states [38]. These criteria define the "preselection" stage of the analysis, and they select samples dominated by DY production. Most events selected at this level pass single-lepton trigger conditions. But, as no specific trigger requirement is made, the trigger acceptance with respect to off-line selections is enhanced to $\approx 92\%$ for the $\mu\mu$ channel and $\approx 100\%$ for the ee and $e\mu$ channels, due to additional events passing lepton+jets or dilepton triggers. The remaining trigger inefficiency is modeled in the simulation by corrections derived from $Z \rightarrow \ell\ell$ samples selected with different trigger requirements. The preselected samples are further subdivided according to the number of jets in the event. Namely 0-, 1-, and (≥ 2)-jet multiplicity bins are considered. Dividing the analysis into different jet multiplicity bins significantly increases the sensitivity of this search as the signal and background compositions are different in each sample.

To correct for any possible mismodeling of the lepton

TABLE I: Observed and expected number of events after preselection in the ee, $e\mu$, and $\mu\mu$ final states. The signal is for a Higgs boson mass of 125 GeV. The uncertainty quoted on the background combines both statistical and systematic uncertainties, after the normalization procedure described in the main text.

	Data	Total background	Signal	$Z/\gamma^\star \to ee$	$Z/\gamma^\star \to \mu\mu$	$Z/\gamma^\star \to \tau\tau$	$t\bar{t}$	W+jets	Diboson	Multijet
ee:	659570	664460 ± 13290	16.1	653263	–	5494	210	795	945	3752
$e\mu$:	14936	15142 ± 303	16.6	408	1211	8671	537	1225	906	2184
$\mu\mu$:	811549	818269 ± 16370	18.7	–	807642	6459	356	438	1314	2060

reconstruction and trigger efficiencies, and to reduce the impact of the luminosity uncertainty, scale factors are applied to the MC samples at the preselection stage to match the data. The Z boson mass peak regions in the preselected samples are used to determine normalization factors. Their differences from unity are found to be consistent with the luminosity uncertainty of 6.1 % [39]. This procedure is repeated for each jet multiplicity to derive jet-bin-dependent DY background normalizations to correct for possible mismodeling of the DY jet multiplicity.

The number of events after the preselection is presented in Table I [40]; all sub-samples are dominated by DY production. Figure 1(a) shows the dilepton invariant mass distributions [40] for data and the background prediction for the combined sub-samples.

ANALYSIS USING DECISION TREES

In the ee and $\mu\mu$ channels, BDTs are trained for each Higgs boson mass value and each jet multiplicity bin to discriminate between the signal and the dominant DY background. The input variables to these "anti-DY BDTs" are kinematic quantities, such as the lepton momenta, the azimuthal opening angle between the two leptons, $\slashed{E}_T$, variables that take into account both $\slashed{E}_T$ and its direction relative to a lepton or a jet, and observables that differentiate between real and misreconstructed $\slashed{E}_T$. This multivariate technique follows the method defined in the previous publication [10] where more details on the BDTs' input variables are given. The final selection stage for the ee and $\mu\mu$ channels is obtained by applying cuts on the anti-DY BDT discriminants [40]. The thresholds are chosen to obtain similar background rejection as the cut-based rejection employed in Ref. [9].

In the $e\mu$ channel the final selection stage requires $M_T^{\min} > 20$ GeV and $M_{T2} > 15$ GeV [40], where $M_T^{\min}$ is the minimum value, over the two possible lepton choices, of the transverse mass, $M_T(\ell, \slashed{E}_T) = \sqrt{2 \cdot p_T^\ell \cdot \slashed{E}_T \cdot [1 - \cos\Delta\phi(\ell, \slashed{E}_T)]}$, and M_{T2} is an extension of the transverse mass suitable for final states with two visible and two invisible particles [41].

The number of events at the final selection stage can be found in Table II, and the distribution of the angular separation between the leptons, combined for all dilepton final states, $\mathcal{R}(\ell^+\ell^-)$, can be seen in Fig. 1(b) [40].

At the final selection stage, a series of new BDTs is built: the "WW-BDTs" are trained to separate the non-resonant WW production from the other backgrounds, while the "final BDTs" are trained to separate the signal from all the backgrounds. In the former case, the Higgs signal is not used in the training. These BDTs rely on the same input variables as for the anti-DY BDTs, but supplementary variables are added characterizing the lepton reconstruction quality and the lepton isolation, to discriminate against the instrumental backgrounds (multijet and W+jets backgrounds). Outputs of jet b-tagging multivariate discriminants [42] are also added as inputs to separate the signal from the $t\bar{t}$ background.

Using the WW-BDT discriminants, we split the 0- and 1-jet samples into WW-depleted and WW-enriched regions for the ee and $\mu\mu$ analyses. In the $e\mu$ channel, splitting only the 0-jet sample according to the lepton reconstruction quality achieves a sufficiently pure separation of the data sample into a WW-depleted and WW-enriched sub-samples. The final BDTs are then trained separately for each jet multiplicity bin, for each dilepton final state, and for the WW-depleted and WW-enriched samples, resulting in 14 BDTs for each mass hypothesis [40]. The outputs of these BDTs are used as final discriminants. Figure 1(c) shows the BDT distributions of the 14 sub-samples summed in bins with similar signal to background ratios (s/b).

SYSTEMATIC UNCERTAINTIES

Systematic uncertainties are estimated for each final state, background, and signal process. They can affect only the normalization or both the normalization and the shape of the final discriminants.

Sources of systematic uncertainty that affect only the normalization arise from the overall normalization uncertainty due to theoretical inclusive cross sections of Z+jets (4%), W+jets (6%), diboson (6%) and $t\bar{t}$ (7%) processes; multijet normalization (30%); the W+jets jet-bin-dependent normalization (15%–30%); the Z+jets jet-bin-dependent normalization (2%–15%); and the modeling of the $\slashed{E}_T$ measurement for the Z+jets background (5%–19%).

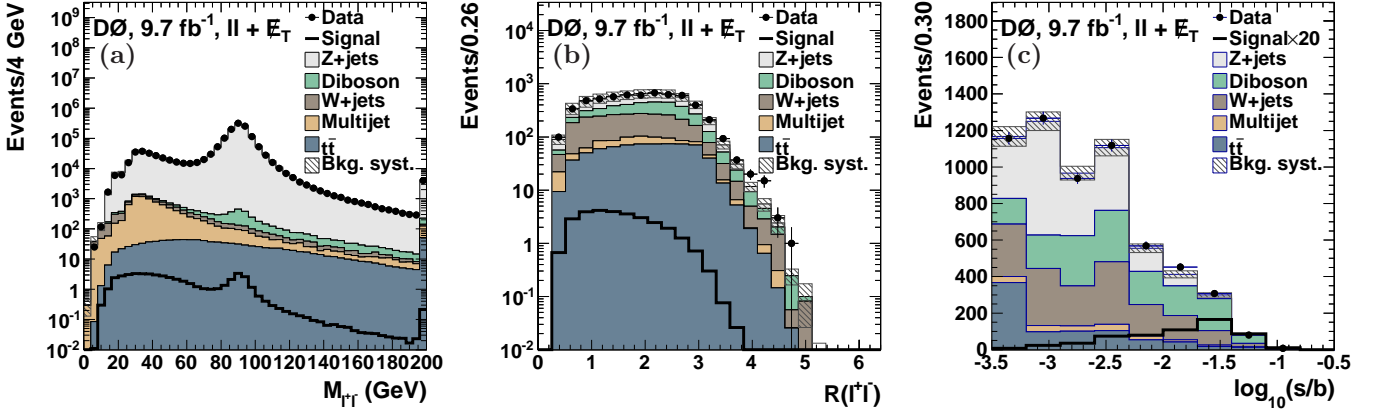The uncertainties on $\sigma(gg \to H)$ production are esti-

FIG. 1: [color online] The (a) dilepton invariant mass at preselection level, (b) the angular separation $\mathcal{R}(\ell,\ell)$ between the leptons at preselection level, and (c) output of the final BDT discriminants after the final selection, sorted as a function of signal over background ratio. In (a), the last bin includes all events above the upper bound of the histogram. In these plots, the hatched bands show the total systematic uncertainty on the background predictions, and the signal distributions are those expected from a Higgs boson of mass $M_H = 125$ GeV. It is scaled by a factor 20 in (c).

TABLE II: Expected and observed number of events after the final selection in the ee, $e\mu$, and $\mu\mu$ final states. The signal is for a Higgs boson mass of 125 GeV. The numbers in parentheses correspond to the efficiency of the final selection with respect to the preselection, shown in Table I, for both the total background and signal. The uncertainty quoted on the total background combines both statistical and systematic uncertainties.

	Data	Total background			Signal		$Z \to ee$	$Z \to \mu\mu$	$Z \to \tau\tau$	$t\bar{t}$	W+jets	Diboson	Multijet
ee:	1882	1859	$\pm$	205	(0.3 %)	7.5 (46.8 %)	746	–	55	151	518	371	18
0 jet	1289	1317	$\pm$	145	(0.2 %)	4.6 (64.8 %)	528	–	32	12	424	307	13
1 jet	379	343	$\pm$	38	(0.4 %)	1.8 (36.6 %)	152	–	6	47	80	53	4
$\geq$ 2 jets	214	199	$\pm$	22	(1.7 %)	1.1 (27.5 %)	65	–	16	91	13	11	1
$e\mu$:	1954	1960	$\pm$	212	(12.9 %)	12.3 (74.1 %)	11	71	11	332	871	628	35
0 jet	1266	1340	$\pm$	129	(10.8 %)	8.0 (82.5 %)	7	55	8	11	716	522	22
1 jet	367	336	$\pm$	43	(16.5 %)	3.1 (67.4 %)	3	13	3	97	116	94	11
$\geq$ 2 jets	321	283	$\pm$	40	(38.1 %)	1.2 (52.2 %)	1	3	1	225	39	12	2
$\mu\mu$:	2057	2109	$\pm$	325	(0.3 %)	9.1 (48.6 %)	–	1055	45	235	231	378	165
0 jet	767	785	$\pm$	100	(0.1 %)	5.1 (57.0 %)	–	210	3	4	178	275	115
1 jet	485	464	$\pm$	72	(0.4 %)	2.3 (43.4 %)	–	238	23	53	42	73	34
$\geq$ 2 jets	805	860	$\pm$	153	(4.9 %)	1.7 (38.2 %)	–	607	19	178	11	30	16

mated following the prescription described in Ref. [43], *i.e.*, by considering as uncorrelated the scale uncertainties of the NNLL inclusive [24, 44], NLO $\geq$ 1 jet [45], and NLO $\geq$ 2 jets [46] cross sections. This prescription results in the following covariance matrix for the the exclusive production of $gg \to H + 0$ jet, $+1$ jet, and $+2$ jets or more , respectively:

$$\begin{pmatrix} (26.6\%)^2 & -(28.3\%)^2 & 0 \\ -(28.3\%)^2 & (41.8\%)^2 & -(20.5\%)^2 \\ 0 & -(20.5\%)^2 & (33.0\%)^2 \end{pmatrix} \quad (1)$$

The PDF uncertainties for $gg \to H$ production, obtained using the prescription from Refs. [24, 45], are 7.6%, 13.8%, and 29.7% for the exclusive production of

$gg \to H + 0$ jet, $+1$ jet, and $+2$ jets or more, respectively.

We also consider sources of systematic uncertainty that affect the shape of the final discriminant distribution (and we quote here the average fractional uncertainty across bins of the final discriminant distribution for all backgrounds): jet energy scale (4%); jet resolution (0.5%); jet identification (2%); jet association to the hard-scatter primary $p\bar{p}$ interaction vertex (2%); b-tagging ($< 2\%$); and W+jets modeling (10%–30%), depending on jet multiplicity bin and final state. The systematic uncertainties due to the modeling of $p_T(WW)$ and $\Delta\phi$ between leptons, and the p_T of the vector boson from the V+jets production, are at the level of $< 1\%$ and taken into account.

MEASUREMENT OF THE NON-RESONANT $p\bar{p} \rightarrow WW$ CROSS SECTION

To validate the analysis techniques employed to search for the Higgs boson, a measurement of the non-resonant WW production cross section is performed. This is motivated by the fact that WW production yields similar particle content and topology as the Higgs boson signal. The same analysis methods are employed as for the Higgs bosons searches, and same sources of systematic uncertainty are accounted for, but the outputs of the WW discriminants, described in the "Analysis using decision trees" section, are considered. The WW cross section is obtained as the result of a maximum likelihood fit to the data, with maximization over the WW signal normalization and over the systematic uncertainties treated as nuisance parameters, as for the SM Higgs boson search results described in the next section. The measurement is carried out using discriminants from the three dilepton final states, in the 0- and 1-jet multiplicity bins. Figure 2 shows the combined output distribution of these discriminants [40], rebinned according to s/b and after the expected backgrounds have been subtracted. The measured value $\sigma_{WW} = 11.6 \pm 0.4\,(\text{stat}) \pm 0.6\,(\text{syst})$ pb [40] is in agreement with the SM prediction of 11.3 ± 0.7 pb [34]. The possible presence of a SM Higgs boson of 125 GeV in the data is not accounted for, but it is expected to bias this measurement upward by ~ 0.1 pb.
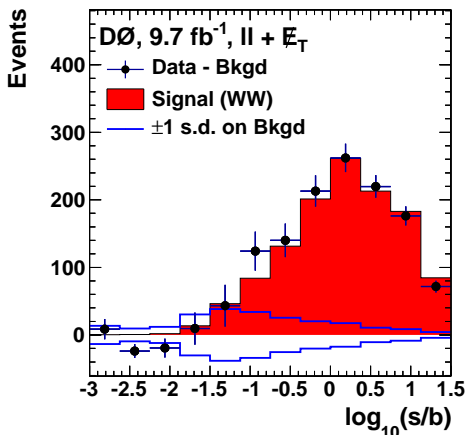
FIG. 2: [color online] The post-fit background-subtracted data distribution for the final discriminant, summed in bins with similar signal to background ratios, for the WW cross section measurement. The uncertainties shown on the background-subtracted data points are the square roots of the post-fit predictions for signal plus background events in each bin, representing the expected statistical uncertainty on the data points. Also shown is the ± 1 s.d. band on the total background after fitting.

SM HIGGS BOSON SEARCH RESULTS

Table II and Fig. 1(c) demonstrate good agreement between the data and the predicted background, in both the numbers of selected events and the distributions of final discriminants. The modified frequentist CL_s method [47] is employed to set limits on SM Higgs boson production, where the test statistic is a log-likelihood ratio (LLR) for the background-only and signal+background hypotheses. The LLR is obtained by summing the LLR values of the bins of the 14 BDT outputs from the different subchannels. In the LLR calculation the signal and background rates are functions of the systematic uncertainties which are taken into account as nuisance parameters with Gaussian priors. Their degrading effect is reduced by fitting signal and background contributions to the data by maximizing the profile likelihood function for the background-only and signal+background hypotheses separately, appropriately taking into account all correlations between the systematic uncertainties [48].

Figure 3(a) shows the LLR values as a function of the tested Higgs boson mass hypothesis. The LLR values expected in the absence of signal and in the presence of a SM Higgs boson of mass 125 GeV are also displayed for comparison. Figure 3(b) [40] presents expected and observed upper limits for $\sigma(p\bar{p} \rightarrow H + X)$ relative to SM predictions. For $M_H = 165$ GeV (125 GeV), the expected limit is 0.76 (3.4) times the SM prediction and the observed limit reaches 0.74 (4.1) in the same units. A SM Higgs boson in the mass range $159 < M_H < 176$ GeV is excluded at the 95% C.L. while the expected exclusion sensitivity is $156 < M_H < 172$ GeV. In these figures, a slight excess of signal-like candidates yields a limit roughly one s.d. above the background expectation, in the mass range $100 < M_H < 145$ GeV. Figure 3(c) shows a comparison of the BDT output distributions, sorted as a function of signal over background ratio, expected for the signal of $M_H = 125$ GeV, and observed in the data after subtracting the fitted backgrounds.

UPPER LIMIT ON $gg \rightarrow H \rightarrow WW$ AND FOURTH GENERATION FERMION INTERPRETATION

Additional generations of fermions can occur naturally in models of grand unification, CP violation, gauge-mediated supersymmetry breaking, and others. Measurements of the Z boson decay width [49] exclude models in which the fourth neutrino mass eigenstate is lighter than 45 GeV, but fourth generation models can still be accommodated for a large fourth-generation neutrino mass. Production of $gg \rightarrow H$ occurs via top-quark loops in the SM. With respect to the SM, the quarks from the fourth generation will provide additional contributions to the quark loop diagram, enhancing production by a factor of 7 to 9, depending on their masses and
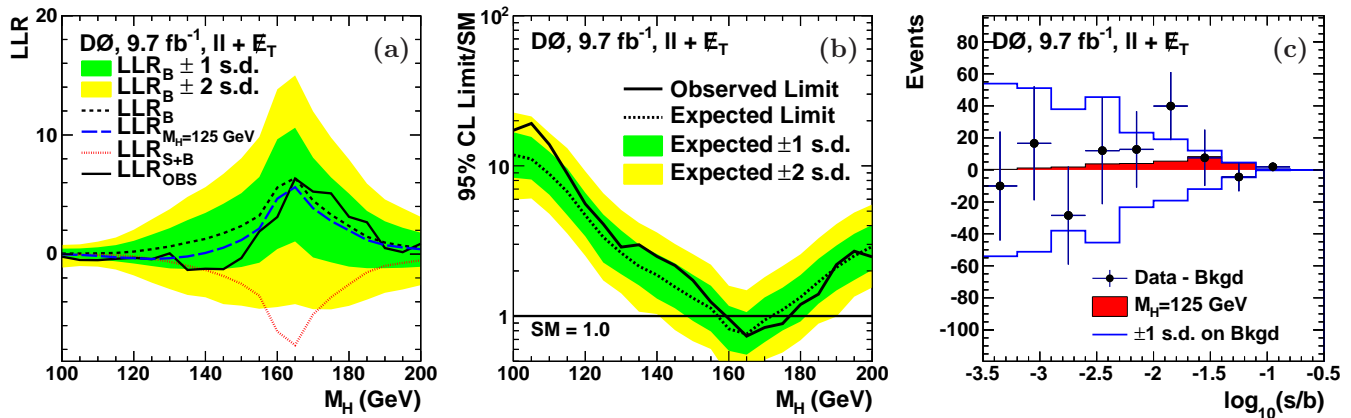
FIG. 3: [color online] (a) The observed LLR as a function of M_H. Also shown are the expected LLRs for the background-only hypothesis, for the signal+background hypothesis, and the expectation in the presence of a signal of $M_H = 125$ GeV. (b) Excluded cross section, $\sigma(p\bar{p} \rightarrow H + X)$, at the 95% C.L. in units of the SM cross section as a function of M_H. In (a) and (b), the green and yellow shaded bands indicate ± 1 and ± 2 s.d. uncertainties of the expected observation for the background-only hypothesis, respectively. (c) Background-subtracted data distribution for the final discriminants, summed in bins with similar signal to background ratios, for $M_H = 125$ GeV. The uncertainties shown on the background-subtracted data points are the square roots of the post-fit background predictions of number of events in each bin, representing the expected statistical uncertainty on the data points. Also shown is the ± 1 s.d. band on the total background after fitting.

the Higgs boson mass [50–52]. A previous combined D0 and CDF result using up to $5.4\,\mathrm{fb}^{-1}$ of data excluded the existence of a SM-like Higgs boson in the mass range between 131 GeV and 204 GeV [53], assuming the presence of a fourth sequential generation of fermions with large masses. Similar searches have been conducted by the ATLAS and CMS Collaborations, yielding and exclusion of $140 < m_H < 185$ GeV [54] and $144 < m_H < 207$ GeV [55], respectively.

To test such models, we derive upper limits on the $gg \rightarrow H \rightarrow WW$ production cross section. The same analysis as described in the previous sections is performed, but the VBF and VH contributions are excluded from the overall signal yield when constructing the LLR. The upper limits are reported in Fig. 4 [40], compared to the expected yield of the $gg \rightarrow H$ production in two models of fourth generation fermions. In the "low-mass" scenario, the masses of the fourth generation charged lepton and neutrino are assumed to be respectively $m_{\ell 4} = 100$ GeV and $m_{\nu 4} = 80$ GeV, just beyond the experimental limits, which yields a reduction by up to 15% in the branching ratio for $H \rightarrow WW$. On the contrary, in the "high-mass" scenario, where $m_{\ell 4} = m_{\nu 4} = 1$ TeV, the leptons are too heavy to contribute to the Higgs boson decay width and the branching ratio for $H \rightarrow WW$ remains basically unchanged relative to the SM branching ratio. For both scenarios, the masses of the fourth-generation down-type (m_{d4}) and up-type (m_{u4}) quarks are fixed to $m_{d4} = 400$ GeV and $m_{u4} = 450$ GeV [50, 51]. From this figure, we derive exclusion of the Higgs boson mass range $125 < M_H < 218$ GeV and $125 < M_H < 228$ GeV, in the low-mass and high-mass scenarios, respectively.
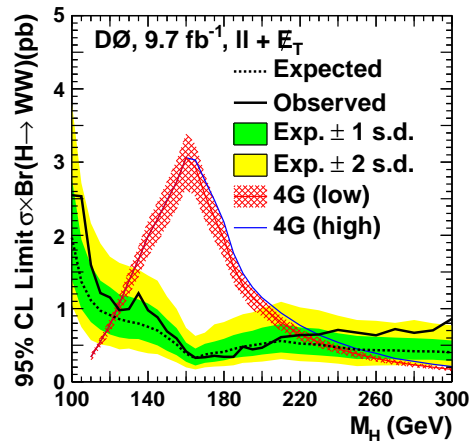

FIG. 4: [color online] Excluded cross section $\sigma(gg \rightarrow H) \times BR(H \rightarrow WW)$ in pb as a function of M_H using all channels. The red and blue lines correspond to the theoretical prediction for a sequential fourth generation assumption in the "low mass" and "high mass" scenarios, respectively (see main text). The hatched region corresponds to the PDF and scale uncertainties on the fourth generation "low mass" prediction [50]. The green and yellow shaded bands indicate ± 1 and ± 2 s.d. uncertainties of the background-only hypothesis, respectively.

FERMIOPHOBIC HIGGS BOSON INTERPRETATION

The mechanism of electroweak symmetry breaking may offer a richer phenomenology than expected in the SM. Several Higgs bosons may exist, or the Higgs bo-

son(s) may have couplings different from those predicted by the SM. In this section, we explore the possibility that the lightest Higgs boson does not couple to fermions at the tree level, but still behaves like the SM Higgs boson for its other properties, in particular for the coupling to vector bosons. In this model, the VBF and VH production have the same cross sections as in the SM. The main consequences of the vanishing fermion couplings are the suppression of production via gluon fusion, and the enhancement of the branching ratios to vector bosons, $H \rightarrow WW$, $H \rightarrow ZZ$, and $H \rightarrow \gamma\gamma$, particularly sizeable below the WW threshold, $m_H < 160$ GeV. To provide masses to the fermions, additional degrees of freedom must exist in the Higgs sector, as predicted in models with Higgs doublets or triplets [56], but it is assumed that those other particles do not have phenomenological impact in our search. In this model, the CMS and ATLAS collaborations exclude a Higgs boson in the mass range $110 < m_H < 194$ GeV [57, 58], while masses below 110 GeV are excluded by LEP experiments [59–62] and Tevatron experiments [63, 64]. The same analysis steps are performed as described for the SM Higgs boson searches, but the various BDTs are retrained, accounting for the fermiophobic Higgs branching ratios, computed using HDECAY, the VBF and VH production at the SM rate, and the suppression of $gg \rightarrow H$ production. The data are in good agreement with background expectation and upper limits on the fermiophobic Higgs are derived, following the same method as for the SM Higgs. They are reported in Fig. 5 [40]. We obtain a cross section upper limit of 3.1 times the fermiophobic Higgs boson production cross section for $M_H = 125$ GeV, while the expected sensitivity is 2.5.
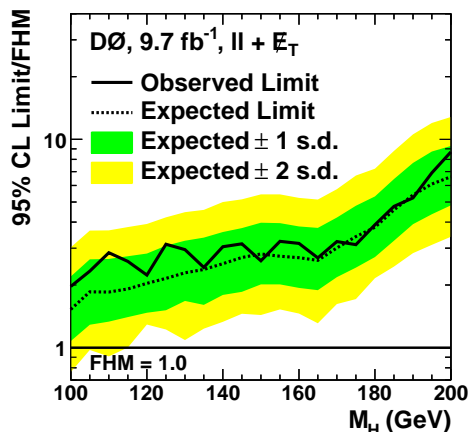
CONCLUSIONS

We have performed a search for Higgs boson production using final states with two oppositely charged leptons and large missing transverse energy in the $e\mu$, ee, and $\mu\mu$ channels. To validate our search methodology we have measured the non-resonant WW production cross section, which yields $\sigma_{WW} = 11.6 \pm 0.7$ pb, in good agreement with the SM prediction of 11.3 ± 0.7 pb. For the Higgs boson searches, we observe agreement between data and the expected backgrounds. We set upper limits on SM Higgs boson production at the 95% C.L. that exclude the mass range $159 < M_H < 176$ GeV, while the expected exclusion sensitivity is $156 < M_H < 172$ GeV. For a mass hypothesis of $M_H = 125$ GeV, we exclude 4.1 times the expected SM Higgs boson production cross section, while the expected sensitivity is 3.4. This upper limit is compatible with the presence of a SM Higgs boson of $M_H = 125$ GeV. We also interpret our search results as cross section upper limit for $gg \rightarrow H$ production, which allows us to exclude the mass range $125 < M_H < 218$ GeV in the context of a fourth generation of fermions. The search results are also interpreted in the framework of a fermiophobic Higgs boson, which yields an exclusion of 3.1 times the fermiophobic Higgs boson production rate for $M_H = 125$ GeV, while the expected sensitivity is 2.5.

FIG. 5: [color online] Excluded cross section, $\sigma(p\bar{p} \rightarrow H + X)$, as a function of M_H using all channels, in units of the Higgs boson production rate expected from the fermiophobic Higgs boson model (FHM) described in the main text.

[1] R. Barate *et al.* [LEP Working Group for Higgs boson searches and ALEPH and DELPHI and L3 and OPAL Collaborations], Phys. Lett. B **565**, 61 (2003).

[2] T. Aaltonen *et al.* [CDF and D0 Collaborations], Phys. Rev. Lett. **104**, 061802 (2010).

[3] The CDF and D0 Collaborations and the Tevatron New Physics and Higgs Working Group, arXiv:1107.5518 (2012).

[4] G. Aad *et al.* [ATLAS Collaboration], Phys. Lett. B **716**, 1 (2012).

[5] S. Chatrchyan *et al.* [CMS Collaboration], Phys. Lett. B **716**, 30 (2012).

[6] T. Aaltonen *et al.* [CDF Collaboration], Phys. Rev. Lett. **109**, 111802 (2012).

[7] V. M. Abazov *et al.* [D0 Collaboration], Phys. Rev. Lett. **109**, 121802 (2012).

[8] T. Aaltonen *et al.* [CDF and D0 Collaborations], Phys. Rev. Lett. **109**, 071804 (2012).

[9] V. M. Abazov *et al.* [D0 Collaboration], Phys. Rev. Lett. **104**, 061804 (2010).

[10] V. M. Abazov *et al.* [D0 Collaboration], Phys. Rev. D **86**, 032010 (2012).

[11] T. Aaltonen *et al.* [CDF Collaboration], Phys. Rev. Lett. **104**, 061803 (2010).

[12] G. Aad *et al.* [ATLAS Collaboration], Phys. Lett. B **716**, 62 (2012).

[13] S. Chatrchyan *et al.* [CMS Collaboration], Phys. Lett. B **710**, 91 (2012).

[14] L. Breiman *et al.*, *Classification and Regression Trees* (Wadsworth, Belmont, CA, 1984); Proceedings of the Thirteenth International Conference, Bari, Italy, 1996, edited by L. Saitta (Morgan Kaufmann, San Francisco, 1996), p. 148.

[15] S. Abachi *et al.*, [D0 Collaboration], Nucl. Instrum. Methods Phys. Res. A **338**, 185 (1994); V. M. Abazov *et al.* [D0 Collaboration], Nucl. Instrum. Meth. in Phys. Res. A **565**, 463 (2006); M. Abolins *et al.*, Nucl. Instrum. Methods Phys. Res. A **584**, 75 (2008); R. Angstadt *et al.*, Nucl. Instrum. Methods Phys. Res. A **622**, 298 (2010).

[16] The pseudo-rapidity is defined as $\eta = -\ln(\tan\theta/2)$, where θ is the polar angle relative to the proton beam direction.

[17] G. C. Blazey *et al.*, arXiv:hep-ex/0005012v2.

[18] Here, $\mathcal{R} = \sqrt{(\Delta\phi)^2 + (\Delta\eta)^2}$, where ϕ is the azimuthal angle around the proton beam direction.

[19] V. M. Abazov *et al.* [D0 Collaboration], Phys. Rev. D **85**, 052006 (2012).

[20] T. Sjöstrand, S. Mrenna, and P. Skands, J. High Energy Phys. **05**, 026 (2006); we use versions 6.319 and 6.413.

[21] M. L. Mangano *et al.*, J. High Energy Phys. **07**, 001 (2003); we use version 2.11.

[22] J. Pumplin *et al.*, J. High Energy Phys. **07**, 12 (2002).

[23] R. Brun and F. Carminati, CERN Program Library Long Writeup W5013, 1993 (unpublished).

[24] D. de Florian and M. Grazzini, Phys. Lett. B **674**, 291 (2009).

[25] P. Bolzoni *et al.*, Phys. Rev. Lett. **105**, 011801 (2011).

[26] J. Baglio and A. Djouadi, J. High Energy Phys. **10**, 064 (2010).

[27] A. D. Martin, W. J. Stirling, R. S. Thorne, and G. Watt, Eur. Phys. J. C **63**, 189 (2009).

[28] G. Bozzi, S. Catani, D. de Florian, and M. Grazzini, Phys. Lett. B **564**, 65 (2003); Nucl. Phys. **B737**, 73 (2006).

[29] A. Djouadi, J. Kalinowski, and M. Spira, Comput. Phys. Commun. **108**, 56 (1998).

[30] R. Hamberg, W. L. van Neerven, and T. Matsuura, Nucl. Phys. **B359**, 343 (1991) [Erratum-ibid. **B644**, 403 (2002)].

[31] V. M. Abazov *et al.* [D0 Collaboration], Phys. Rev. Lett. **100**, 102002 (2008).

[32] K. Melnikov and F. Petriello, Phys. Rev. D **74**, 114017 (2006).

[33] U. Langenfeld, S. Moch and P. Uwer, Phys. Rev. D **80**, 054009 (2009); we use $\sigma(t\bar{t}) = 7.04$ pb.

[34] J.M. Campbell and R.K. Ellis, Phys. Rev. D **60**, 113006 (1999); we use MCFM version 6.0. We use $\sigma(WW) = 11.34$ pb, $\sigma(WZ) = 3.22$ pb, and $\sigma(ZZ) = 1.20$ pb as calculated for $75 < M_Z < 105$ GeV.

[35] T. Melia, P. Nason, R. Rontsch, and G. Zanderighi, J. High Energy Phys. **1111**, 078 (2011).

[36] S. Frixione and B.R. Webber, J. High Energy Phys. **06**, 029 (2002).

[37] T. Binoth, M. Ciccolini, N. Kauer, and M. Krämer, J. High Energy Phys. **03**, 065 (2005); J. High Energy Phys. **12**, 046 (2006).

[38] V. M. Abazov *et al.* [D0 Collaboration], Paper in preparation.

[39] T. Andeen *et al.* [D0 Collaboration], FERMILAB-TM-2365; B. C. K. Casey *et al.* [D0 Collaboration], Nucl. Instrum. Meth. A **698**, 208 (2013).

[40] See Auxiliary Material part for additional plots and tables supporting the textual descriptions of the analysis.

[41] C. G. Lester and D. J. Summers, Phys. Lett. B **463**, 99 (1999); H. Cheng and Z. Han, J. High Energy Phys. **12**, 063 (2008).

[42] V. M. Abazov *et al.* [D0 Collaboration], Nucl. Instrum. Meth. in Phys. Res. A **620**, 490 (2010). An updated version of this algorithm was used.

[43] I. W. Stewart and F. J. Tackmann, Phys. Rev. D **85**, 034011 (2012).

[44] C. Anastasiou, R. Boughezal and F. Petriello, J. High Energy Phys. **04**, 003 (2009).

[45] C. Anastasiou, G. Dissertori, M. Grazzini, F. Stöckli, and B. R. Webber, J. High Energy Phys. **08**, 099 (2009).

[46] J. M. Campbell, R. K. Ellis, and C. Williams, Phys. Rev. D **81**, 074023 (2010).

[47] T. Junk, Nucl. Instrum. Meth. in Phys. Res. A **434**, 435 (1999); A. Read, J. Phys. G **28**, 2693 (2002).

[48] W. Fisher, FERMILAB-TM-2386-E (2006).

[49] ALEPH, DELPHI, L3, OPAL, and SLD Collaborations, LEP Electroweak Working Group, and SLD Electroweak and Heavy Flavor Groups, Phys. Rep. **427**, 257 (2006).

[50] C. Anastasiou, R. Boughezal and E. Furlan, J. High Energy Phys. **1006**, 101 (2010).

[51] G. D. Kribs, T. Plehn, M. Spannowsky, and T. M. P. Tait, Phys. Rev. **D76**, 075016 (2007).

[52] E. Arik, O. Cakir, S. A. Cetin, and S. Sultansoy, Acta Phys. Polon. **B37**, 2839 (2006).

[53] T. Aaltonen *et al.* [CDF and D0 Collaborations], Phys. Rev. D **82**, 011102 (2010).

[54] G. Aad *et al.* [ATLAS Collaboration], Eur. Phys. J. C **71**, 1728 (2011).

[55] S. Chatrchyan *et al.* [CMS Collaboration], Phys. Lett. B **699**, 25 (2011).

[56] A. Barroso, L. Brucher, and R. Santos, Phys. Rev. D **60**, 035005 (1999); J. Gunion, R. Vega, and J. Wudka, Phys. Rev. D **42**, 1673 (1990); A. G. Akeroyd, Phys. Lett. B **368** (1996); A. G. Akeroyd, M. A. Diaz, M. A. Rivera and D. Romero, Phys. Rev. D **83**, 095003 (2011).

[57] S. Chatrchyan *et al.* [CMS Collaboration], J. High Energy Phys. **09**, 111 (2012).

[58] G. Aad *et al.* [ATLAS Collaboration], Eur. Phys. J. C **72**, 2157 (2012).

[59] A. Heister *et al.* [ALEPH Collaboration], Phys. Lett. B **544**, 16 (2002).

[60] J. Abdallah *et al.* [DELPHI Collaboration], Eur. Phys.

J. C **35**, 313 (2004).

[61] P. Achard *et al.* [L3 Collaboration], Phys. Lett. B **534**, 28 (2002); Phys. Lett. B **568**, 191 (2003).

[62] G. Abbiendi *et al.* [OPAL Collaboration], Phys. Lett. B **544**, 44 (2002).

[63] T. Aaltonen *et al.* [CDF Collaboration], Phys. Rev. Lett. **103**, 061803 (2009).

[64] V. M. Abazov *et al.* [D0 Collaboration], Phys. Rev. Lett. **107**, 151801 (2011).

Auxiliary Material

To appear as an Electronic Physics Auxiliary Publication (EPAPS).

Tables and distributions after the preselection

TABLE III: Expected and observed numbers of events after the preselection in the ee, $e\mu$, and $\mu\mu$ final states in the different jet multiplicity bins. The signal is for a Higgs boson mass of 125 GeV.

	Data	Total background			Signal	$Z \to ee$	$Z \to \mu\mu$	$Z \to \tau\tau$	$t\bar{t}$	W+jets	Diboson	Multijet
ee:												
0 jet	572831	575445	±	11509	7.1	566846	–	4727	15	623	517	2718
1 jet	75326	77130	±	4628	5.0	75162	–	663	66	143	243	853
≥ 2 jets	11413	11885	±	1783	4.0	11256	–	105	129	29	185	181
eμ:												
0 jet	12131	12361	±	247	9.7	348	1043	7546	16	972	728	1709
1 jet	2039	2040	±	122	4.6	51	139	946	155	191	153	406
≥ 2 jets	766	741	±	111	2.3	9	29	180	366	63	25	70
μμ:												
0 jet	699513	701663	±	14033	8.9	–	693390	5663	9	343	673	1585
1 jet	95615	98840	±	5930	5.3	–	97278	686	87	78	329	382
≥ 2 jets	16421	17766	±	2665	4.5	–	16974	110	260	16	313	94

Event yields after the preselection are shown in Table III. The distributions of the dilepton invariant mass (Fig. 6), angular separation between the leptons (Fig. 7) and missing transverse energy (Fig. 8) show the good agreement between the data and the simulation after the preselection in the ee, $e\mu$ and $\mu\mu$ channels. Figures 9 and 10 show the distributions of the Drell-Yan (DY) BDT discriminants for the ee and $\mu\mu$ channels respectively. Figure 11 shows the distributions of the variables $M_T^{\min}$ and M_{T2}, used by the $e\mu$ channel to reject the DY background. The distributions of the dilepton invariant mass (Fig. 12), angular separation between the leptons (Fig. 13) and missing transverse energy (Fig. 14) are shown for the ee, $e\mu$ and $\mu\mu$ channels after the final selection. The final discriminant distributions for the three channels are shown in Figs. 15, 16 and 17. Figure 18 shows the background-substracted data distributions of the final discriminants for $M_H = 125$ GeV and $M_H = 165$ GeV. Tables IV, V and VI give the expected and observed upper limits at the 95% C.L. for Higgs boson production in the SM, in models with a fourth generation of fermions and assuming fermiophobic couplings, respectively. Figures 19, 20 and 21 show the WW discriminant distributions for the ee, $e\mu$ and $\mu\mu$ channels. Figure 22 shows the distribution of the combination of WW discriminants for the ee, $e\mu$ and $\mu\mu$ channels. The results of the $p\bar{p} \to WW$ cross section measurement for the ee, $e\mu$ $\mu\mu$ channels, and their combination are shown in Fig. 23.
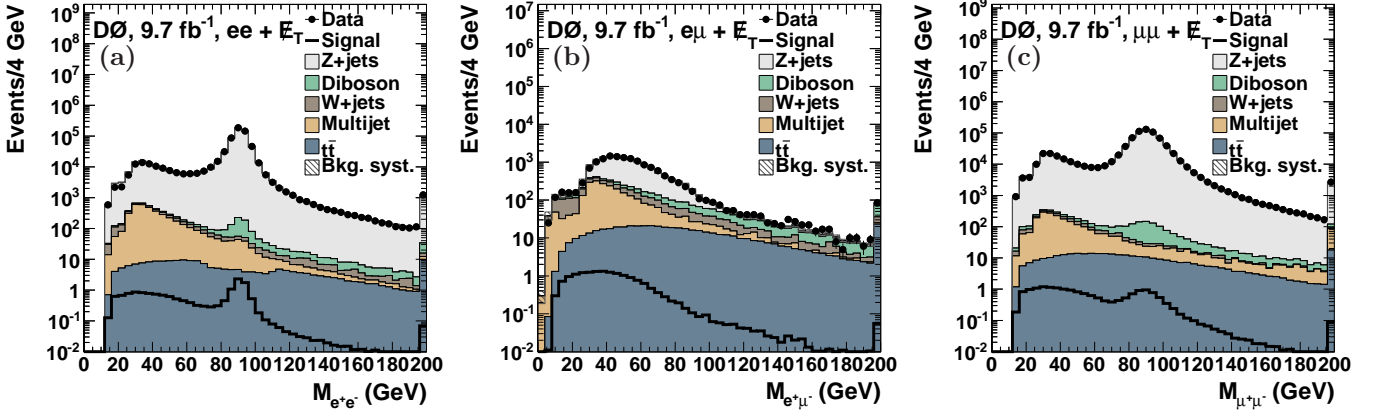
FIG. 6: Distributions of the dilepton invariant mass for the (a) *ee* channel, (b) *eµ* channel, and (c) *µµ* channel after the preselection. In (a), (b) and (c) the last bin includes all events above the upper bound of the histogram. In these plots, the hatched bands show the total systematic uncertainty on the background predictions, and the signal distributions are those expected from a Higgs boson of mass $M_H = 125$ GeV.
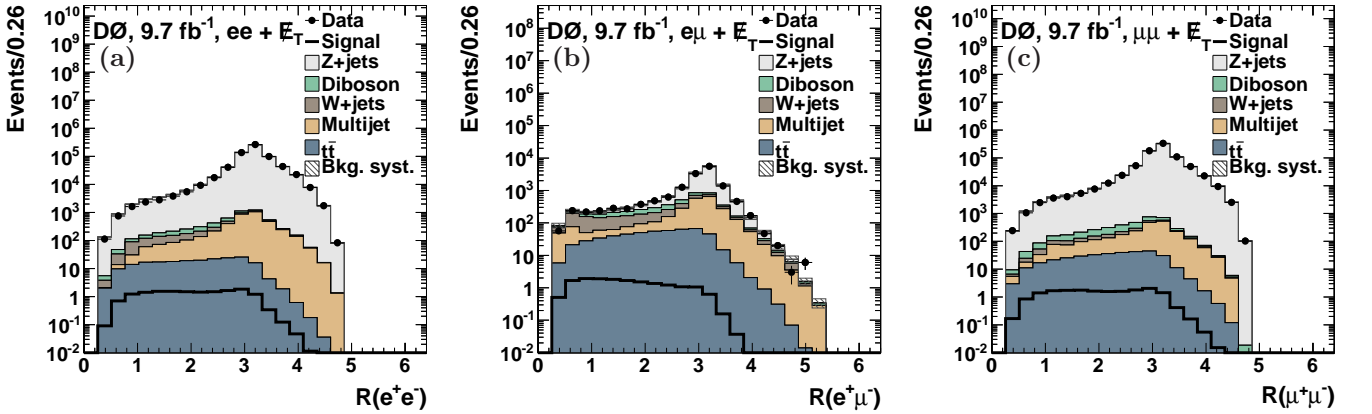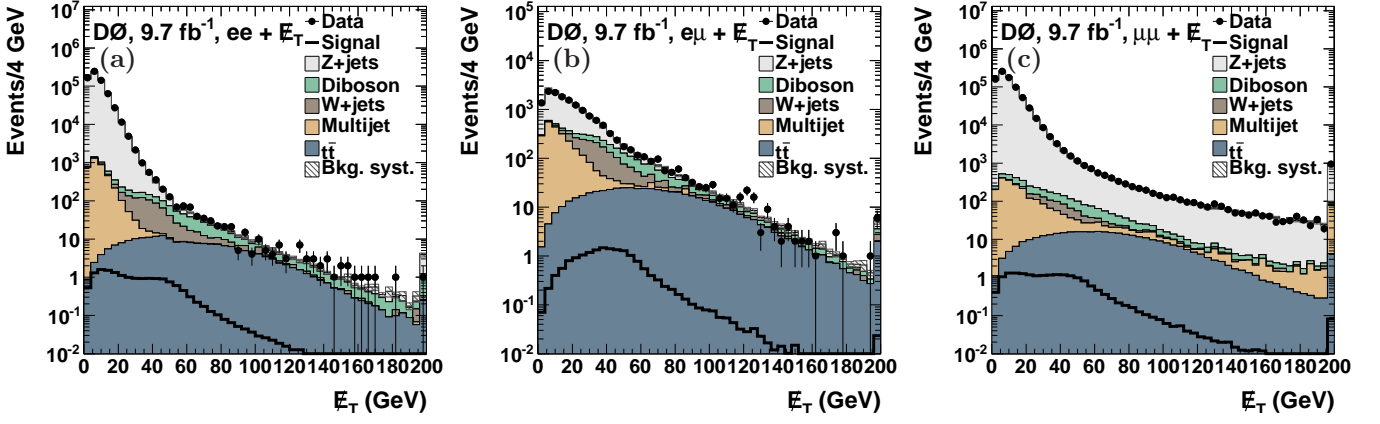

FIG. 7: Distributions of the angular separation $\mathcal{R}(\ell,\ell)$ between the leptons for the (a) *ee* channel, (b) *eµ* channel, and (c) *µµ* channel after the preselection. In these plots, the hatched bands show the total systematic uncertainty on the background predictions, and the signal distributions are those expected from a Higgs boson of mass $M_H = 125$ GeV.

FIG. 8: Distributions the missing transverse energy for the (a) *ee* channel, (b) *eμ* channel, and (c) *μμ* channel after the preselection. In (a), (b) and (c) the last bin includes all events above the upper bound of the histogram. In these plots, the hatched bands show the total systematic uncertainty on the background predictions, and the signal distributions are those expected from a Higgs boson of mass $M_H = 125$ GeV.
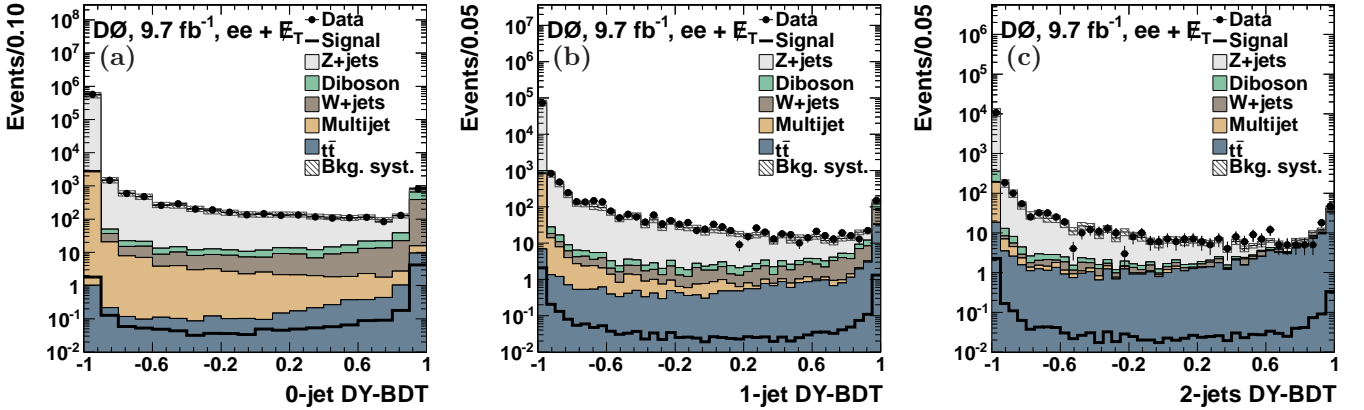
FIG. 9: Distributions of the Drell-Yan (DY) BDT discriminant for *ee* channel in the (a) 0-jet bin, (b) 1-jet bin, and (c) $\geq$ 2-jets bin. The BDTs are trained for a Higgs mass of 125 GeV. The signal distributions are those expected from a Higgs boson of mass $M_H = 125$ GeV.
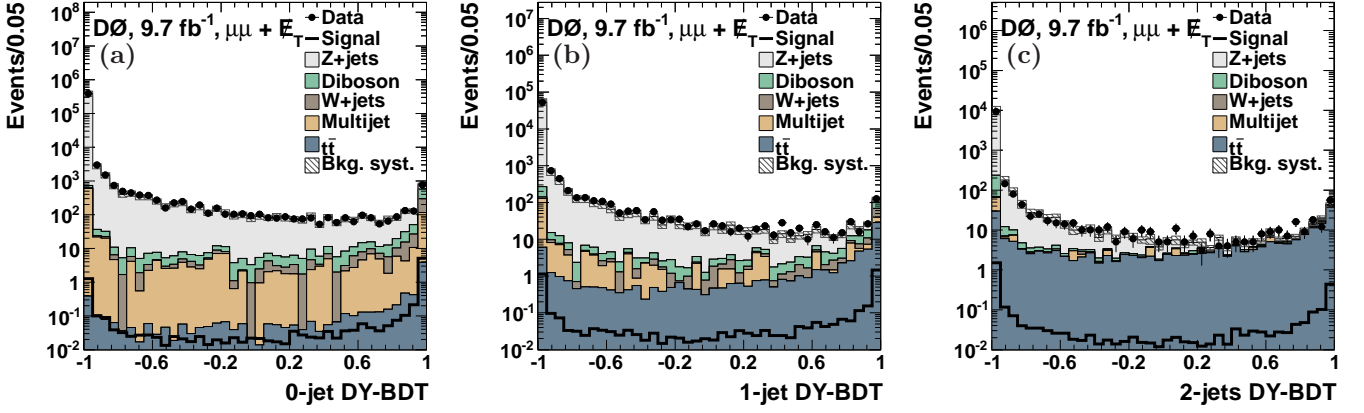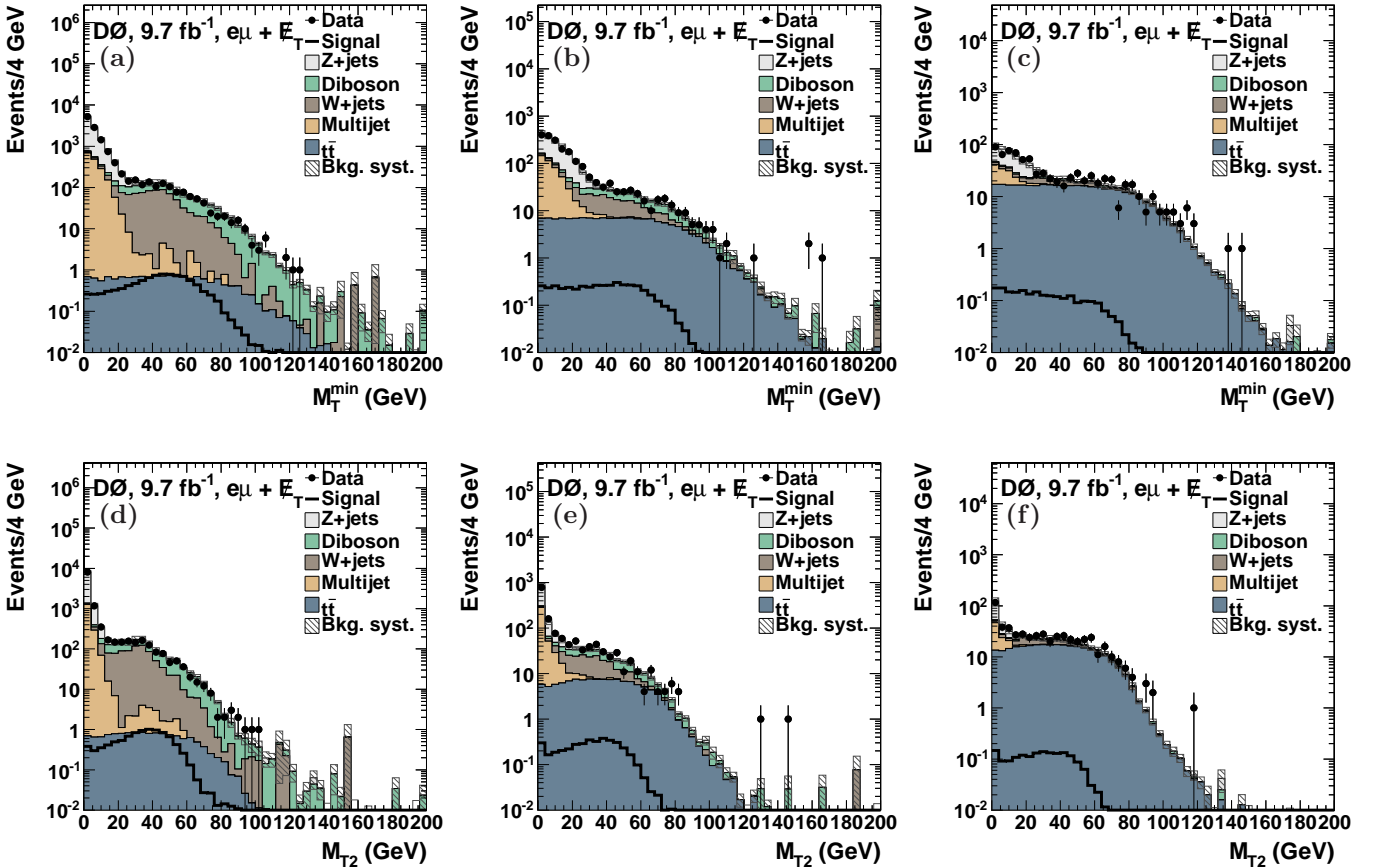
FIG. 10: Distributions of the DY BDT discriminant for $\mu\mu$ channel in the (a) 0-jet bin, (b) 1-jet bin, and (c) $\geq$ 2-jets bin. The BDTs are trained for a Higgs mass of 125 GeV. The signal distributions are those expected from a Higgs boson of mass $M_H = 125$ GeV.

FIG. 11: $M_T^{\min}$ distribution for the $e\mu$ channel in the (a) 0-jet bin, (b) 1-jet bin, and (c) $\geq$ 2-jets bin. M_{T2} distribution for the $e\mu$ channel in the (d) 0-jet bin, (e) 1-jet bin, and (f) $\geq$ 2-jets bin. For both distributions, the signal distributions are those expected from a Higgs boson of mass $M_H = 125$ GeV.

Distributions at the final selection level
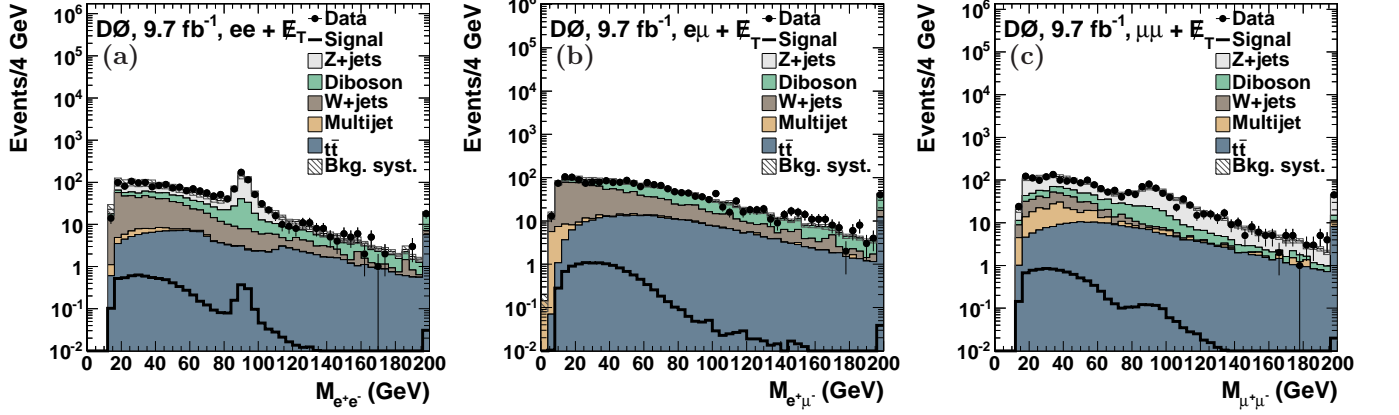
FIG. 12: Distributions of the dilepton invariant mass for the (a) ee channel, (b) $e\mu$ channel, and (c) $\mu\mu$ channel after the final selection. In (a), (b) and (c) the last bin includes all events above the upper bound of the histogram. In these plots, the hatched bands show the total systematic uncertainty on the background predictions, and the signal distributions are those expected from a Higgs boson of mass $M_H = 125$ GeV.
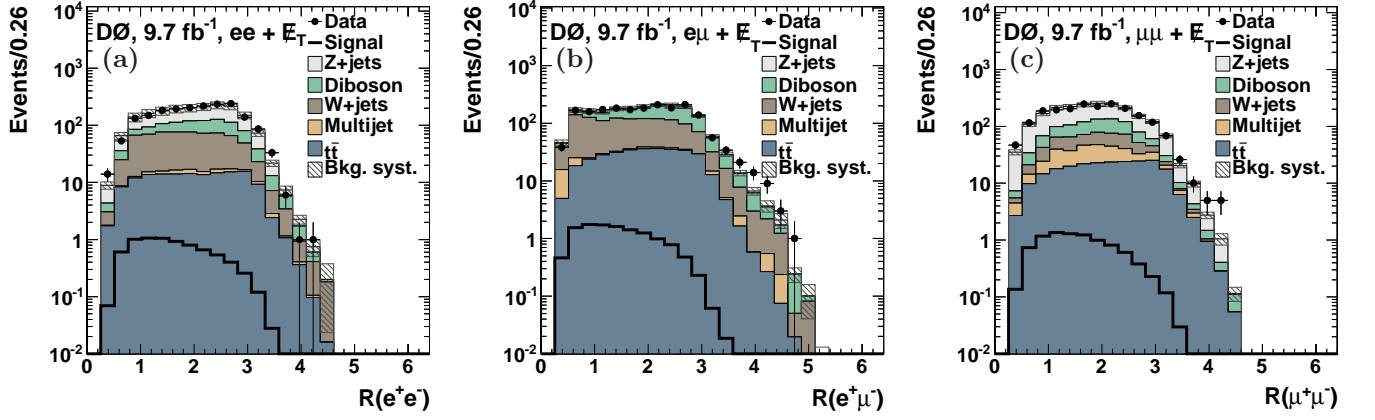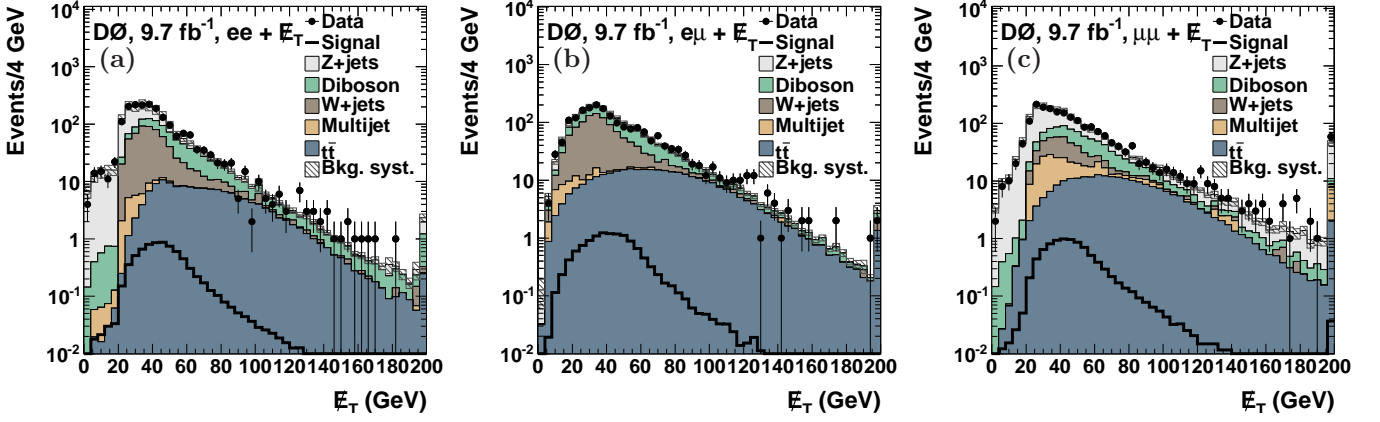

FIG. 13: Distributions of the angular separation $\mathcal{R}(\ell, \ell)$ between the leptons for the (a) ee channel, (b) $e\mu$ channel, and (c) $\mu\mu$ channel after the final selection. In these plots, the hatched bands show the total systematic uncertainty on the background predictions, and the signal distributions are those expected from a Higgs boson of mass $M_H = 125$ GeV.

FIG. 14: Distributions of the missing transverse energy for the (a) *ee* channel, (b) *eµ* channel, and (c) *µµ* channel after the final selection. In (a), (b) and (c) the last bin includes all events above the upper bound of the histogram. In these plots, the hatched bands show the total systematic uncertainty on the background predictions, and the signal distributions are those expected from a Higgs boson of mass $M_H = 125$ GeV.
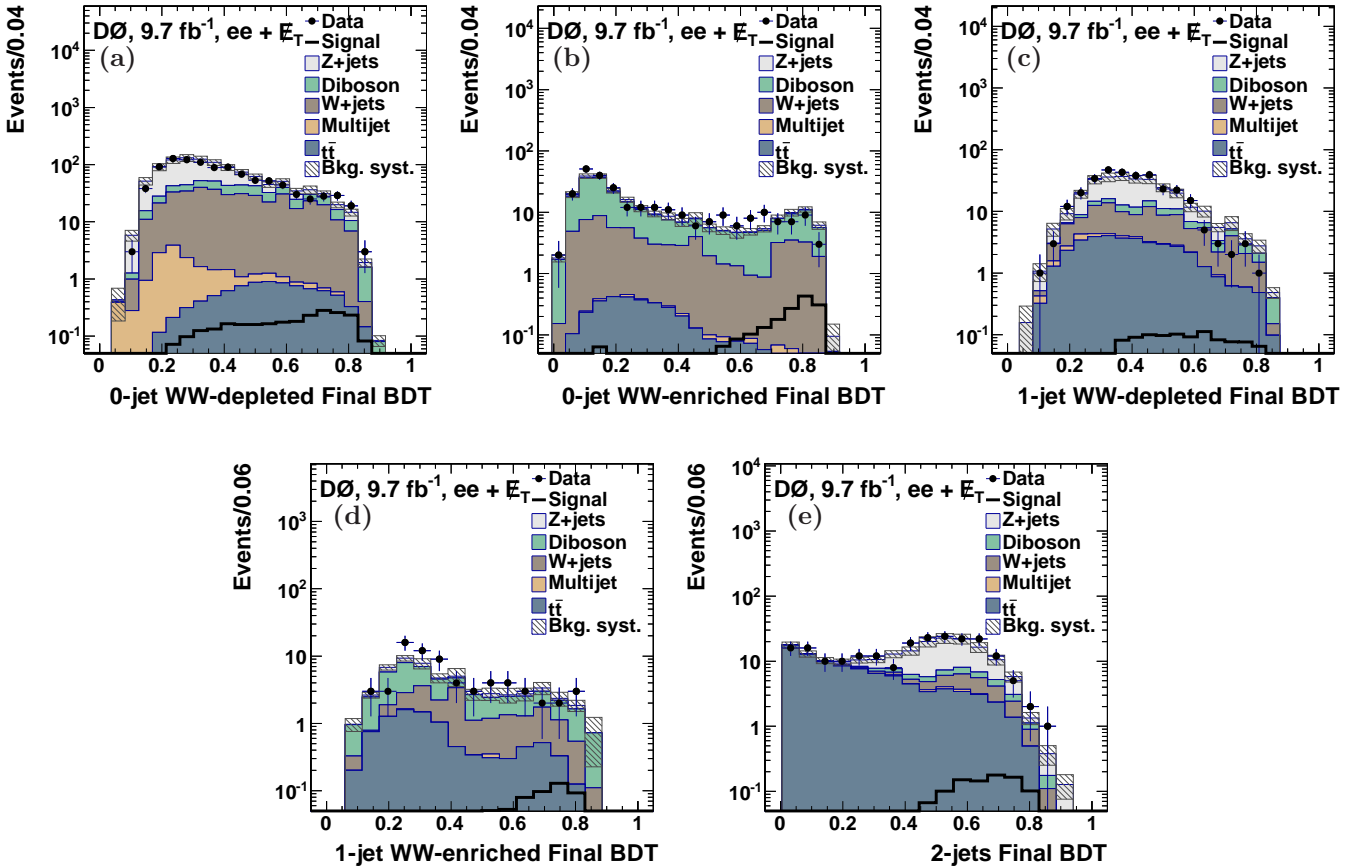

FIG. 15: Distributions of the final BDT discriminant for $M_H = 125$ GeV for the *ee* channel with (a) 0-jet WW-depleted, (b) 0-jet WW-enriched, (c) 1-jet WW-depleted, (d) 1-jet WW-enriched, and (e) $\geq$ 2-jets.
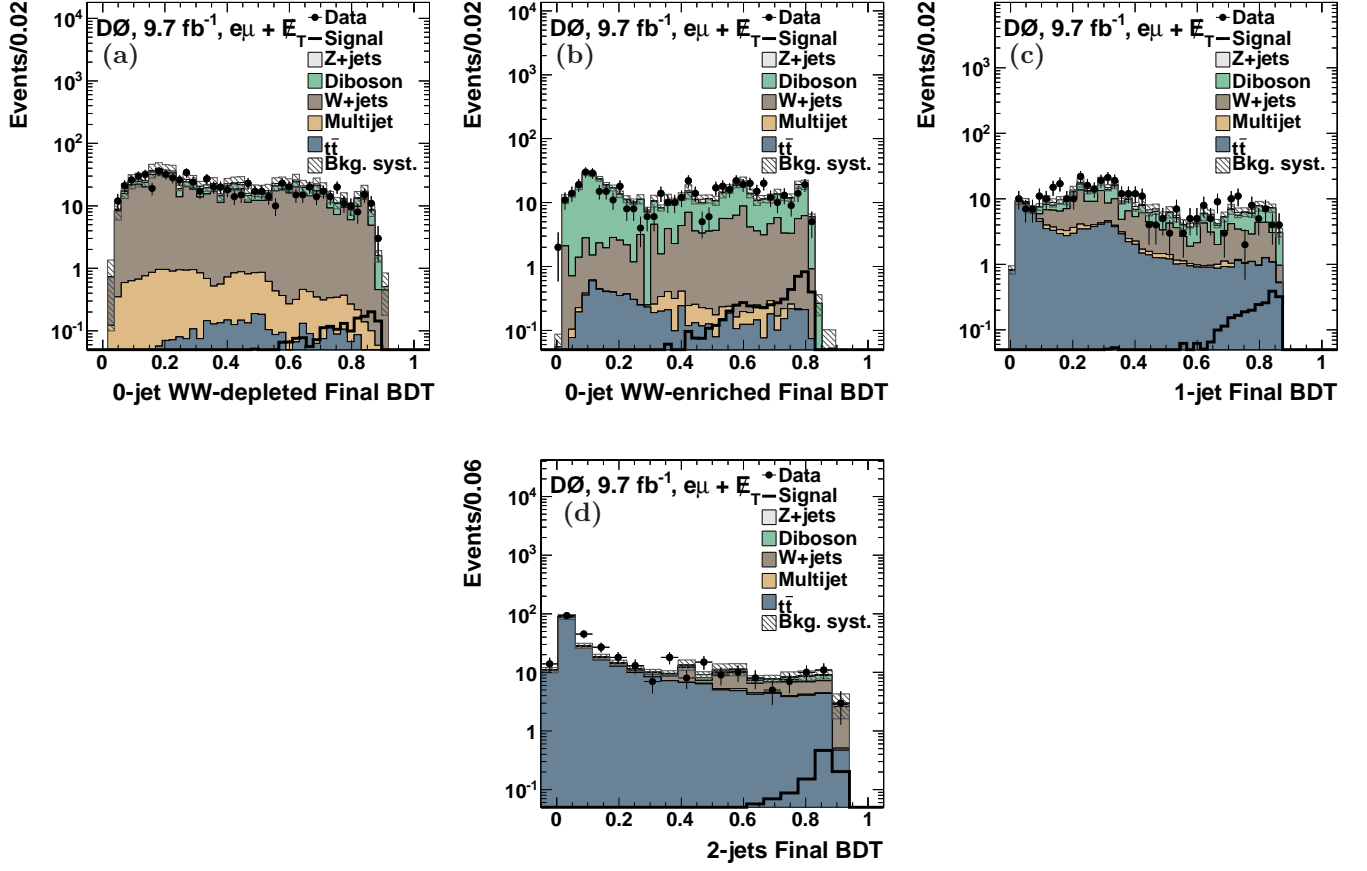
FIG. 16: Distributions of the final BDT discriminant for $M_H = 125$ GeV for the $e\mu$ channel with (a) 0-jet WW-depleted, (b) 0-jet WW-enriched, (c) 1-jet , and (d) $\geq$ 2-jets.
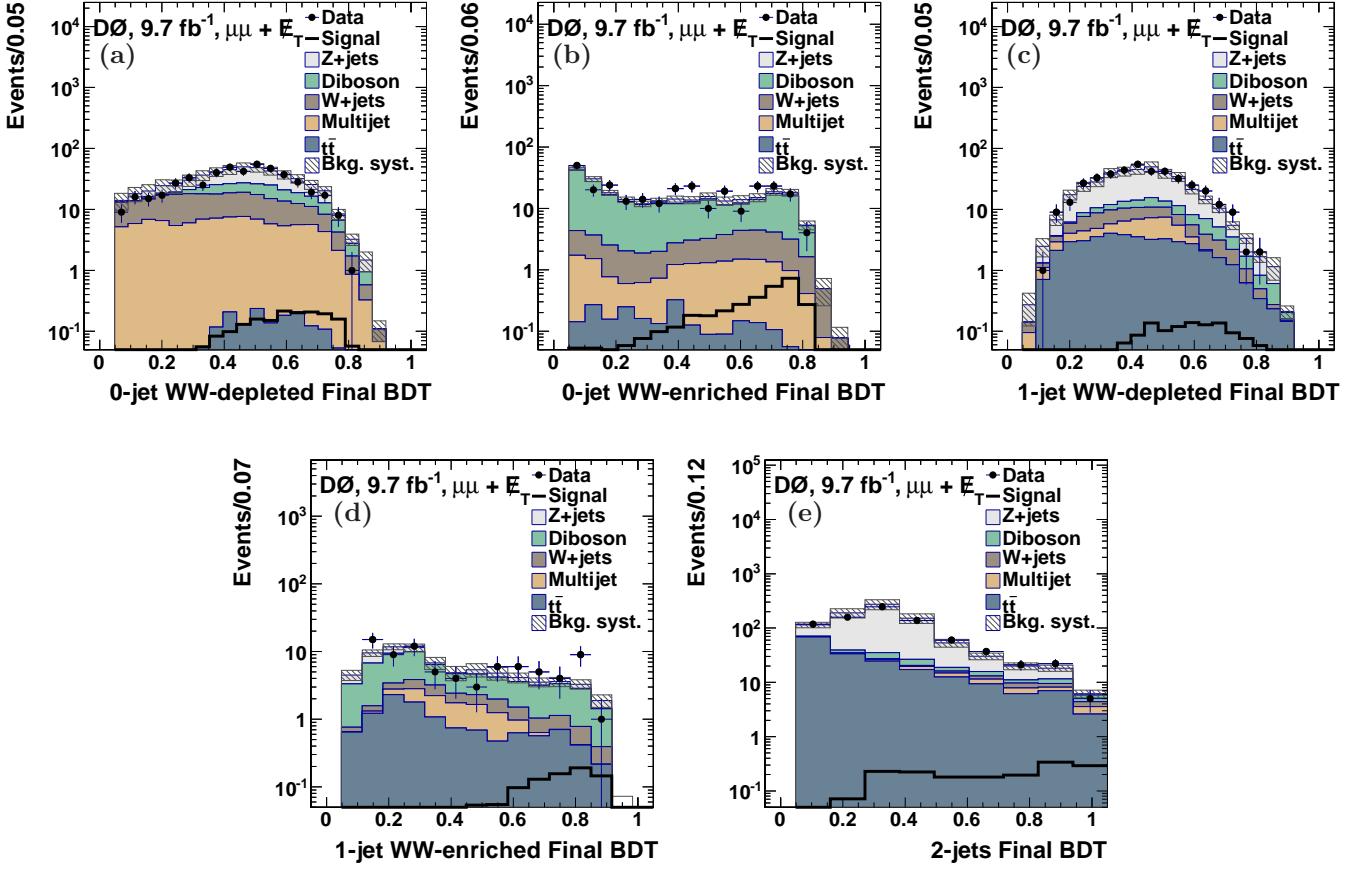
FIG. 17: Distributions of the final BDT discriminant for $M_H = 125$ GeV for the $\mu\mu$ channel with (a) 0-jet WW-depleted, (b) 0-jet WW-enriched, (c) 1-jet WW-depleted, (d) 1-jet WW-enriched, and (e) $\geq$ 2-jets.
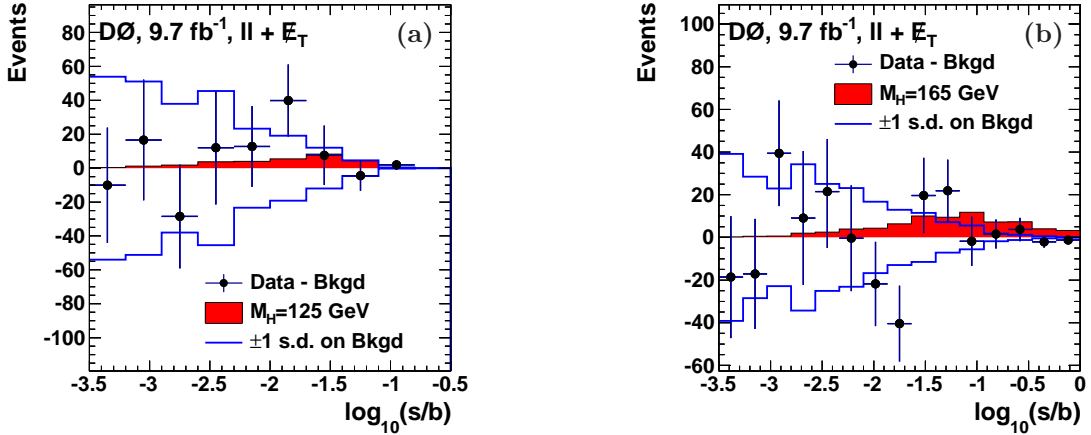

FIG. 18: The background-subtracted data distributions for the final discriminants, summed in bins with similar signal to background ratios, for (a) $M_H = 125$ GeV, and (b) $M_H = 165$ GeV. The uncertainties shown on the background-subtracted data points are the square roots of the post-fit background number of events predictions in each bin, representing the expected statistical uncertainty on the data. Also shown is the ± 1 s.d. band on the total background after fitting.

Tables of limits for the different searches

TABLE IV: Expected and observed upper limits at the 95% C.L. for $\sigma(p\bar{p} \to H+X)$ relative to the SM for the total combination, and separately for the ee, $e\mu$, $\mu\mu$ channels and different Higgs boson masses.

M_H (GeV)	100	105	110	115	120	125	130	135	140	145	150	155	160	165	170	175	180	185	190	195	200
Exp. all:	11.8	11.1	8.84	6.73	4.70	3.36	2.64	2.15	1.88	1.56	1.32	1.13	0.82	0.76	0.94	1.10	1.34	1.69	2.11	2.52	2.91
Obs. all:	17.2	19.1	13.9	8.85	5.58	4.10	2.88	2.99	2.50	2.17	1.73	1.24	0.96	0.74	0.84	0.89	1.20	1.40	2.20	2.71	2.48
Exp. ee.	13.6	14.2	13.5	13.0	10.1	7.21	5.56	4.32	3.86	3.22	2.77	2.30	1.76	1.64	1.94	2.24	2.72	3.44	4.12	4.90	5.65
Obs. ee	20.6	23.6	16.9	15.1	8.41	6.25	4.67	5.05	3.80	3.98	3.13	2.70	2.11	1.79	2.02	2.31	2.68	3.21	5.53	5.76	5.76
Exp. $e\mu$	42.4	27.9	15.9	10.0	6.55	4.65	3.63	2.97	2.48	2.02	1.77	1.50	1.11	1.06	1.28	1.51	1.75	2.27	2.80	3.30	3.75
Obs. $e\mu$	28.1	20.0	12.5	7.95	6.23	4.75	3.39	2.88	2.61	2.14	1.75	1.28	1.00	0.86	1.17	1.33	1.79	2.16	2.68	3.31	3.20
Exp. $\mu\mu$	39.4	29.0	20.6	13.9	8.76	6.25	4.72	3.95	3.39	3.09	2.59	2.31	1.74	1.61	1.95	2.30	2.89	3.49	4.40	5.05	5.83
Obs. $\mu\mu$	66.8	68.2	53.1	27.4	16.8	10.1	8.22	7.65	6.77	5.53	5.01	3.95	3.01	2.31	2.53	2.79	3.51	4.14	5.85	7.45	7.92

TABLE V: Expected and observed upper limits at 95% CL for $\sigma(gg \to H) \times BR(H \to WW)$ in pb, for the combination of the ee, $e\mu$, $\mu\mu$ channels and different Higgs boson masses.

M_H (GeV)	100	105	110	115	120	125	130	135	140	145	150	155	160	165	170	175
Exp. all:	1.97	1.37	1.11	0.97	0.91	0.85	0.82	0.80	0.75	0.70	0.61	0.51	0.38	0.32	0.37	0.40
Obs. all:	2.55	2.53	1.60	1.21	1.15	0.98	1.00	1.21	0.98	0.88	0.69	0.59	0.42	0.33	0.34	0.36

M_H (GeV)	180	185	190	195	200	210	220	230	240	250	260	270	280	290	300
Exp. all:	0.41	0.45	0.48	0.50	0.52	0.56	0.52	0.51	0.47	0.44	0.43	0.43	0.42	0.42	0.40
Obs. all:	0.34	0.34	0.48	0.44	0.47	0.61	0.64	0.65	0.71	0.67	0.63	0.72	0.67	0.70	0.86

TABLE VI: Assuming fermiophobic couplings, expected and observed upper limits for $\sigma(p\bar{p} \to H + X)$ relative to the fermiophobic Higgs expected yields for the combination of the ee, $e\mu$, $\mu\mu$ channels and different Higgs boson masses.

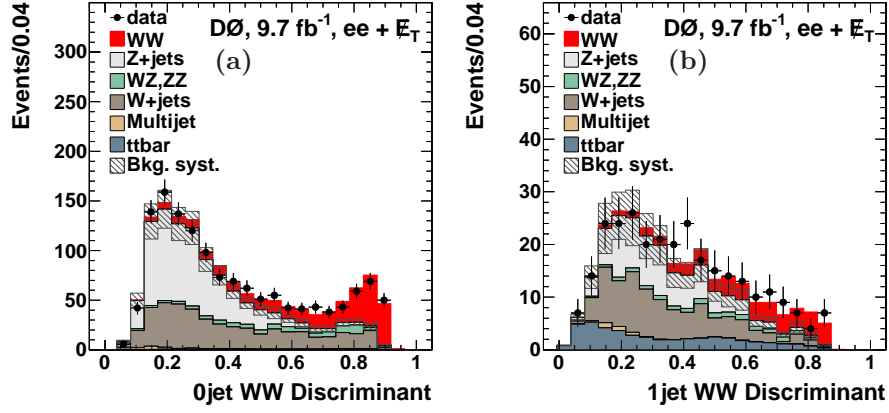| M_H (GeV)	100	105	110	115	120	125	130	135	140	145	150	155	160	165	170	175	180	185	190	195	200
Exp. all:	1.53	1.85	1.85	1.91	2.03	2.15	2.29	2.37	2.53	2.71	2.81	2.75	2.70	2.62	3.01	3.41	3.78	4.58	5.40	6.10	6.60
Obs. all:	1.97	2.33	2.85	2.59	2.23	3.14	2.96	2.42	3.05	3.15	2.61	3.24	3.16	2.70	3.23	3.12	3.89	4.76	5.23	6.90	8.70

WW cross section measurement

FIG. 19: The WW discriminant distributions in the ee channel for (a) no jet and (b) one jet.
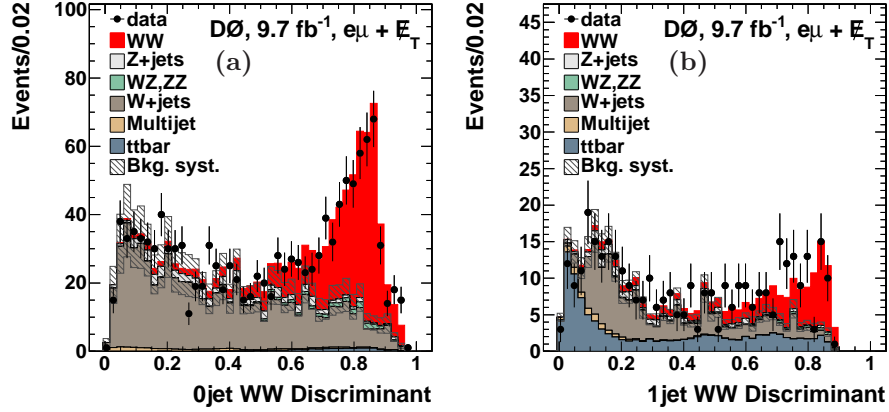

FIG. 20: The WW discriminant distributions in the $e\mu$ channel for (a) no jet and (b) one jet.
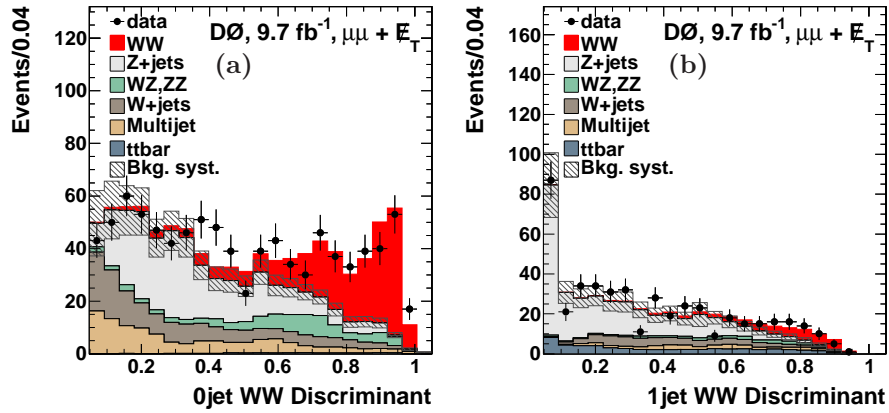

FIG. 21: The WW discriminant distributions in the $\mu\mu$ channel for (a) no jet and (b) one jet.
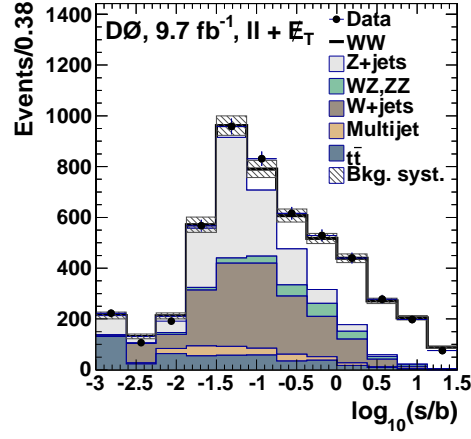
FIG. 22: Distribution of the combination of WW discriminants from ee, $e\mu$, and $\mu\mu$ channels employed to measure the WW cross section, sorted as a function of signal over background ratios. The hatched bands show the total systematic uncertainty on the background prediction.
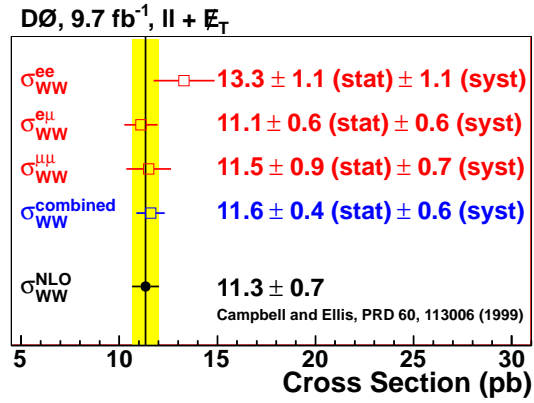

FIG. 23: Results of the $p\bar{p} \rightarrow WW$ cross section measurements in each dilepton final state and their combination.